Contents

1 Interaction Region Development

1.1 Interaction Region Design Concept

The design parameters of eRHIC and their rationale have been discussed in Sections **??**. Some parameters relevant for the interaction region design are repeated in Table 1 for convenience.

Table 1: Key beam parameters at the energy point of highest luminosity relevant for the interaction region design.

	Proton	Electron	Proton	Electron	Proton	Electron
E_{CM} [GeV]	105		140		28	
Energy [GeV]	275	10	275	18	41	5
ϵ_x [nm]	9.0	20.0	9.6	22.0	45.9	20.0
ϵ_y [nm]	1.3	1.0	5.7	3.3	2.6	2.0
β_x^* [cm]	213	96	213	96	95	218
β_y^* [cm]	4.0	5.0	4.0	5.0	4.0	5.0

The layout of the interaction region (IR) fulfills the following requirements:

- To achieve small beam cross sections and high luminosity, the beams are strongly focused at the interaction point (small β^*) by low-β-quadrupole magnets (also referred to as final focus quadrupoles).

- The final focus quadrupoles must have sufficient aperture for the large beam size at their location.

- Large contributions to the chromaticity, which is a set of parameters characterizing the energy sensitivity of the beam optics, are generated in the low-β quadrupoles. Chromaticity needs to be compensated by nonlinear sextupole fields which, in turn, limit the dynamic aperture. The IR design balances small β^* and tolerable values of chromaticity.

- The colliding beam detector requires a large acceptance of protons scattered off the collision point. Therefore, we do not place accelerator components inside the detector ($\pm 4.5\,\mathrm{m}$ from the IP). The low-β quadrupoles have a large aperture so that scattered protons and neutrons can be detected by detector elements placed further downstream.

- The beam divergence (and the minimum β^*) is restricted to enable detection of forward scattered protons with transverse momentum as small as $p_t = 200\,\mathrm{MeV/c}$. These particles are then outside the $10\,\sigma$ proton beam envelope and are detectable by near-beam-detectors, so-called "Roman Pots", which are placed on the forward hadron beam pipe.

- The beams collide under a crossing angle of 22 mrad to separate the electron and proton beams quickly, to avoid parasitic collisions and to provide space for a neutron detector in the forward [1] direction and the luminosity detector in the forward electron direction. An important factor is the large bunch frequency (up to 112 MHz, which corresponds to only 9 ns bunch spacing) required for high luminosity. The crossing angle effects (enlarged transverse beam size and excitation of synchro-betatron resonances) must be compensated for by using so-called crab cavities, transverse RF resonators which kick the head and the tail of the proton (and electron) bunches in opposite directions in the plane of the crossing angle. These cavities are placed at a horizontal betatron phase advance of $\pi/2$ from the interaction point (IP) on both the rear- and the forward side, forming a 180° bump. This causes the bunches to be tilted in the horizontal plane by exactly half the crossing angle at the IP, and provides (ideally) the same collision geometry as head-on collisions thereby avoiding synchrobetatron coupling.

- Strong synchrotron radiation which might be generated by the electron beam can destroy sensitive detector equipment and make data-taking impossible. Therefore, we argue that the electron beam must not experience dipole fields in the interaction region (IR), certainly not upstream of the IP (we use the term forward side). This is another strong reason why the two beams must collide at a crossing angle. Synchrotron radiation generated in the low-β quadrupoles on the rear-electron side should be absorbed on the rear side of the IR as far as possible from the detector so as to minimize backscattered photons. This requires an extra large aperture for the electron low-β quadrupole magnets on the downstream side of the IP.

- Both the hadron and electron beams are spin polarized. Polarization is only stable if the polarization direction coincides with the direction of the guide field in the arc. In collisions, the spins are oriented longitudinally. Thus the IR design accommodates pairs of spin rotators which accomplish longitudinal spin at the IP and vertical spin in the arcs. The spin rotators in the hadron ring already exist and are unchanged in this design. The spin rotators for the electron beam consist of two pairs of strong solenoids with quadrupole magnets in-between each pair which are tuned such that the x-y coupling by the two solenoids cancels. This set of four solenoids is required on both sides of the IP. The beam transport between the rotators is "spin transparent". This means that the magnetic fields in quadrupole magnets experienced by a particle performing betatron and synchrotron oscillations cancel between the spin rotators. This translates into beam optics spin matching conditions.

- The IR layout must provide room for a luminosity monitor on the rear side. This monitor detects hard γ-rays that are generated in the Bethe-Heitler process and exploited for luminosity measurement. The dipole magnet bending the electrons away from the path of the γ beam is at the same time a spectrometer magnet for the off-momentum electrons generated by the Bethe-Heitler process.

- On the forward proton side, a neutron spectrometer is required. A dipole magnet bends the hadron beam away from the collision axis to provide space for this ele-

---

[1] The IP separates the IR into a forward and a rear side or direction. The forward side is the side of the proton beam coming from the IP and the rear side is the side of protons going to the IP.

ment. It also generates dispersion which helps to detect forward scattered protons in detectors that are integrated into the hadron beam pipe (called "Roman Pots")

The purpose of the interaction region (IR) is to focus the beams to small spot sizes at the collision point and to separate them into their respective beam lines while providing the space and geometry required by the physics program for the detector. The separation is accomplished by a total crossing angle of 22 mrad between the two beams, which has the advantage of avoiding the introduction of separator dipoles in the detector vicinity that would generate huge amounts of synchrotron radiation. The detrimental effects of this crossing angle on the luminosity and beam dynamics are compensated by a crab-crossing scheme.

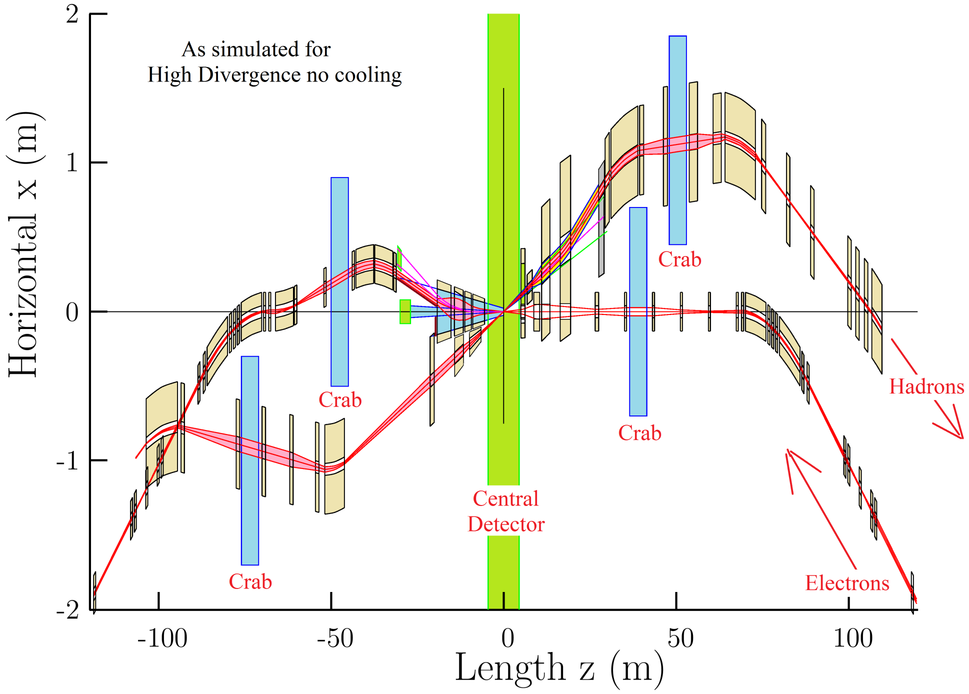

Figure 1: Schematic layout of the interaction region (top view). Beams cross with a crossing angle of 22 mrad. Note the length scales for the horizontal and vertical axis are very different. The IR design integrates focusing magnets for both beams, luminosity and neutron detectors, electron taggers, spectrometer magnets, near-beam detectors (Roman pots for hadrons), crab cavities, and spin rotators for both beams. The two beams are focused by quadrupole doublets. On the hadron-forward side, there are separate focusing magnets which are longitudinally interleaved. The first quadrupole magnet for electrons is integrated into a hadron spectrometer dipole. On the rear side, hadrons and electrons are focused by quadrupoles which are installed side-by-side in the same cryostat. The β-functions in the IR remain with maximum β for hadrons of 1600 m within the operating range of RHIC and the maximum β-functions for electron remain below 400 m, except for the horizontal β on the rear side.

The Figures 1 and 2 show different parts of the separate hadron and electron IR layouts as they were separately simulated for dynamic aperture and spin performance. They will, however, need to be modified to resolve some conflicts and other changes prior to the next iteration:

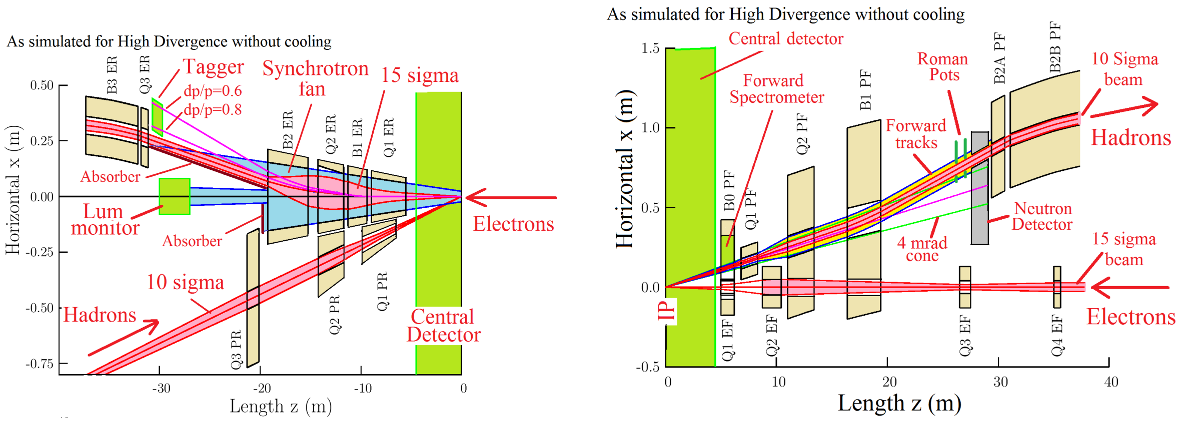

Figure 2: A zoom of the interaction region layout in the rear (left) and forward (right) directions.

1. On the rear side (at z=-100) the hadron and electron rings are on top of each other. The hadron ring at that location is matched into an existing RHIC dipole, while the electron ring is displaced as part of its needed spin rotation. One, or both, these rings will have to be relocated.

2. . The magnet designs for the first rear side hadron (Q1PR) and electron (Q1ER) quadrupoles were conceived as being housed in the same yoke with twin tapered apertures and twin tapered coils. In the designs shown in these figures the first electron quad, but not the hadron one, has been moved further from the IP generating an unacceptable displacement between them. These hadron and electron magnets will be brought back into alignment, keeping now smaller distances between Q1 and Q2, and probably moving B1ER and merging it with B2ER.

3. Dipole magnet B1PF, originally located close to quadrupole Q2PF is shown approximately 3 m further downstream. This results in an uncomfortably small separation between the hadron beam (and its Roman pot detectors) and neutron cone (and its neutron detector). B1PF will be move back close to Q2PF to increase this spacing.

4. The designs for several of the early forward hadron quadrupoles (Q1PF, Q2PF, and B1PF) are made difficult by the near location of the electron beam that must be free of significant stray fields from the proton magnets. To ease these difficulties, it has been tentatively decided to increase the crossing angle from 22 to 25 mrad. This change will also help the rear magnets referred to in item number 2, and free up space for needed correction coils. The change will require an 11% increase in the crab cavity voltages, but this is well within their design capabilities.

It is not expected that any of these changes will have significant impacts on dynamic apertures and spin effects.

The small β-functions at the interaction point (IP) necessitate focusing elements as close as possible to the IP. This is accomplished by a combination of dual-aperture magnets and an interleaved arrangement of single-aperture quadrupoles with minimized outer radii, as shown in Figures 1. The magnets use active shielding as demonstrated at BNL for an ILC IR application. Design magnet apertures are chosen such that a minimum aperture radius of 10σ for protons and 15σ for electrons is ensured in all operating modes. Tables 2 and 3 list the magnet parameters in the electron and proton beam lines and their positions, beginning from the interaction point (IP).

Table 2: Forward hadron and electron magnets.

FORWARD DIRECTION [2]	Hadron Magnets				Electron Magnets	
	B0	Q1PF	Q2PF	B1	Q0EF	Q1EF
Start position [m]	5.0	6.8	11.0	13.9	5.0	8.74
End position [m]	6.2	8.3	13.4	16.9	6.2	10.46
Length [m]	1.2	1.5	2.4	3.0	1.2	1.72
Position w.r.t. electron IP obit [cm]	11.0	15.4	26.4	34.6	0.0	0.4
Angle w.r.t. electron IP orbit [mrad]	0.0	22.0	20.0	22.0	0.0	0.0
Inner radius [cm]	17.0	4.2	10.5	13.5	2.2	4.85
Outer radius [cm]	47.0	12.8	21.5	29.5	5.0	14.7
Peak field [T]	1.3	5.641	4.622	4.574	0.309	0.282
Gradient [T/m]	0.0	-131.0	44.13	0.0	-14.061	5.996

Table 3: Rear hadron and electron quadrupoles with their apertures tapered in proportion to their distance to the IP.

REARWARD DIRECTION	Hadron Magnets		Electron Magnets			
	Q1PR	Q2PR	Q1ER	B1ER	Q2ER	B2ER
Start position [m]	5.5	11.67	5.5	9.35	11.67	15.22
End position [m]	8.92	14.24	8.92	11.24	14.24	19.22
Length [m]	3.42	2.57	3.42	1.89	2.57	4.00
Position w.r.t. electron IP obit [cm]	-12.1	-25.8	2.8		3.5	
Angle w.r.t. electron IP orbit [mrad]	-22.0	-22.0	-7.3		10.0	
Entrance radius [cm]	2.09	4.50	5.76	9.64	0.71	14.04
Exit radius [cm]	3.39	5.49	7.95	11.06	11.35	17.04
Peak field [T]	1.73 – 2.81	2.47 – 3.01	0.29 – 0.40	0.164	0.41 – 0.48	0.164
Gradient [T/m]	-82.90	54.86	-5.06	0.0	4.23	0.0

Since for both beams the vertical IP β-function is much smaller than the horizontal one, $\beta_y^* \ll \beta_x^*$, the innermost quadrupoles in either beam line are vertically focusing. In the hadron ring this limits the maximum vertical β-function in those magnets to about 1600 m at a proton beam energy of 275 GeV, resulting in moderate contributions to the overall chromaticity of the machine. The horizontal β-function is intentionally increased to about 1200 m in the reqion of the crab cavities. This limits the required voltage of those devices, which scales as $1/\sqrt{\beta_x^* \beta_{\mathrm{crab},x}}$, to about $U_{\mathrm{crab}} = 14\,\mathrm{MV}$. At lower energies the IP β-functions are increased, resulting in lower β-functions in the low-β magnets as well as at the crab cavities. However, due to the lower beam rigidity the required crab cavity voltage does not exceed 14 MV at any energy.

The focusing scheme for the electrons is conceptually the same as for the hadrons. The vertical β-function reaches a maximum of about 500 m in the low-β quadrupoles, while the horizontal β is intentionally increased to about 200 m at the crab cavities to limit their required voltage.

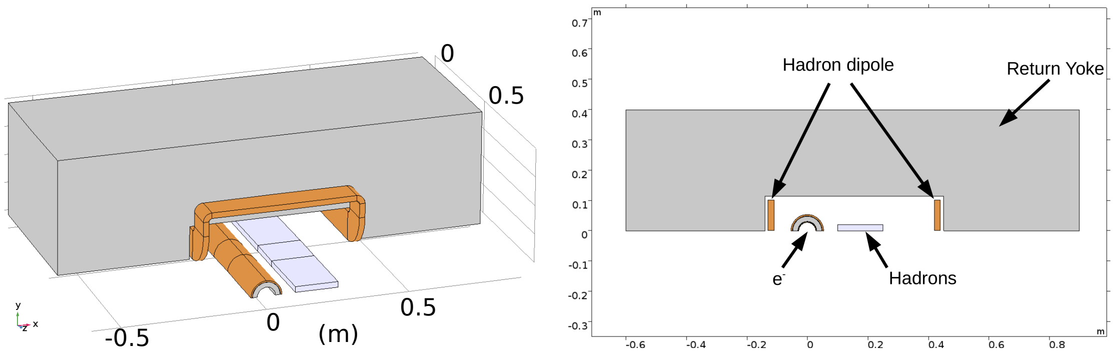

Figure 3: Schematic drawing of the warm iron B0 spectrometer dipole with the superconducting 1.3 T bucking coil shielding the electron beam, and the electron quadrupole Q0EF inside that bucking coil

The forward hadron magnet apertures are completely dominated by experimental acceptance requirements, and the 10 σ outline shown for the circulating beam only uses the small central regions of the magnet apertures. This allows particles scattered at small angles to pass through the apertures of the innermost magnets so they can be detected by detectors which are integrated into the hadron beam vacuum system ("Roman Pots") further down the beamline.

The B0 spectrometer magnet shown in Figure 3 is used to cover an intermediate experimental acceptance region between what can be detected in the main solenoid detector and that corresponding to particles that will exit through the IR magnets. Inside its aperture the electron beam is shielded by a 2 m long superconducting bucking coil (dipole active shield magnet) with an outside diameter of 10 cm and a field of 1.3 T. This bucking coil houses the vertically focusing superconducting electron low-β quadrupole Q0EF, as shown on Figure 4.

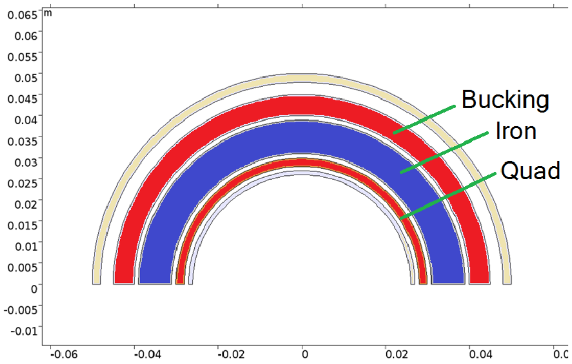

Figure 4: Design of the electron quadrupole Q0EF with its 1.3 T bucking coil to shield the electron beam from the B0 spectrometer magnet

The superconducting proton low-β quadrupole Q1PF, and possibly also Q2PF, are equipped with an anti-quadrupole and an iron shield in order to reduce the stray field strength experienced by the nearby electron beam to acceptable levels. Figure 5 (left) shows a cross section of the vertically focusing proton quad Q1PF. The horizontally focusing quadrupole Q2PF could be conceptionally very similar; alternatively, a design as depicted in Figure 5 (right) might be used. The horizontally focusing electron quadrupole

Q1EF uses a rather conventional superconducting design.

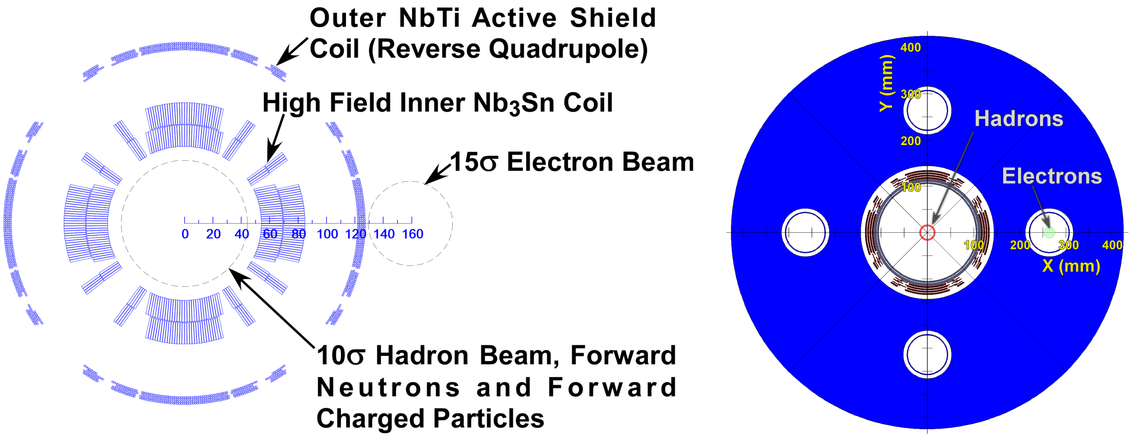

Figure 5: Left: Q1PF actively shielded coil configuration. Right: Large aperture Q2PF hadron quadrupole with passively shielded cutout region in yoke for the electron beam

The B1 dipole separates the hadron beam from the outgoing 4 mrad neutron cone, and creates dispersion at the Roman Pots to allow determination of the forward momentum of the scattered particles.

The electron beamline on the forward side does not contain any bending magnets within 80 m upstream of the IP. Within this region the only source of synchrotron radiation is focusing in quadrupole magnets. The synchrotron radiation fan generated in the far away arc dipoles can be easily collimated such that it is completely contained within the radiation fan produced by the quadrupoles in the straight. Provided the beam is collimated to its $13\,\sigma$ bounds, this fan has finite maximum divergences that are allowed to pass, without interference, through the beam pipe and following magnets, thus allowing for installation of detector components close to the beam. This is discussed in detail in Section **??**.

On the rearward side, no dipoles are introduced into the proton beam line, which allows placement of the low-β quadrupoles even closer to the IP than on the forward side. The electron beamline contains a bending magnet that bends the electrons away from the γ beam generated by scattering of electrons at the hadrons (Bethe-Heitler process) which is used to measure luminosity in the luminosity monitor placed in this area. The bending magnet also serves as a spectrometer to tag scattered electrons that lost energy in the Bethe-Heitler process. However, since this magnet is introduced downstream of the main detector the associated synchroron radiation fan does not pass through the experiment.

The vertically focusing low-β quadrupoles Q1ER and Q1PR are realized as a superconducting dual-aperture magnet sharing the same iron yoke, as shown in Figure 6 (left). The apertures for both beams are both tapered and angled with respect to each other, following the divergent proton beam and synchrotron radiation fan as they emerge from the central detector, as depicted in Figure 6 (right). The tapering is needed to minimize the initial magnet apertures and to allow enough iron between the beams in order to limit the

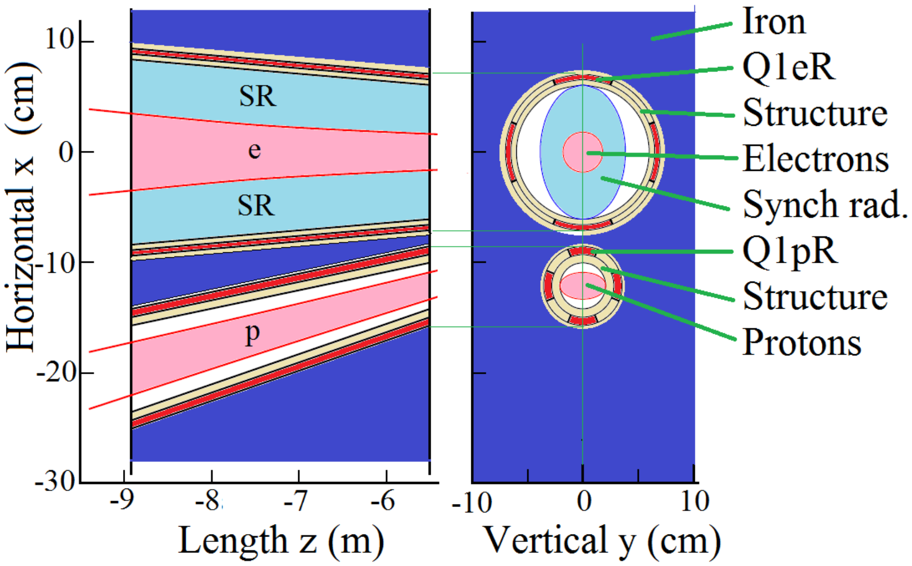

Figure 6: Cross section and top view of the first rear quadrupoles Q1ER and Q1PR, sharing the same iron yoke. The proton quadrupole Q1PR is equipped with an anti-quadrupole to shield the nearby electrons from stray fields. The apertures are tapered around the synchrotron radiation fan and the proton beam envelope, respectively.

magnetic fields for each of them effecting the other.

The required horizontal aperture radius $x_{\rm synch}$ to accommodate the synchrotron radiation fan from the 15σ electron beam at distance s from the IP is parametrized as

$$x_{\rm synch}(s) = 6.75 \times 10^{-3}(s + 3.5) \qquad (1)$$

The vertical size of the synchrotron radiation fan $y_{\rm synch}$ is significantly smaller than the horizontal one. The horizontally focusing quadrupoles Q2ER and Q2PR are conceptually similar to Q1ER and Q1PR, but may not require tapering of the beam apertures due to the larger distance between the two beams. With these apertures, the entire synchrotron radiation fan is transported safely through the interaction region until it hits a dedicated absorber 23 m from the IP.

1.2 IR Vacuum Design

The interface requirements within the interaction region (IR) present several complex challenges which require close attention to detail. The vacuum chamber in this region will become the primary interface between the particle beams and the detectors used to study their interactions.

One of the first challenges is to meet all of the geometrical requirements of the region. First and foremost the vacuum chamber must be designed to allow clear passage of the two high energy particle beams. Allowances for the synchrotron radiation (SR) fan resulting from the strong focusing electron quadrupoles also need to be taken into account. Designing the central vacuum pipe with a large diameter would easily meet these requirements and it would provide a large conductance to the vacuum pumps which are required to achieve the lowest possible pressure in the detector region. However, since some of the resulting products of the collisions decay extremely fast, detectors must be placed as close as possible to the interaction point. Since these particles must pass through the walls of the beam pipe, every effort must be made to minimize their interaction.

Further complicating the geometry is the fact that the charged particle beams induce electromagnetic fields in the walls of the vacuum chambers. These induced fields create an image current which is floating inside the vacuum chamber walls and travels with the particle bunches as they move through the accelerator. Changes in the material resistivity or abrupt steps result in wake fields which can retard the image current and lead to energy loss and heating of the vacuum system.

Every effort must be made to reduce the dynamic pressure inside the IR vacuum chamber in order to minimize beam-gas interactions. The particles in the circulating beams can be scattered by residual gas molecules, which results in high background levels. Any synchrotron radiation (direct or scattered) impinging on surfaces will result in a high dynamic pressure which further increases the beam-gas interaction problem and the background signal of the detector.

1.2.1 Geometry

In order to start developing an acceptable envelope for the IR vacuum chamber, a full scale layout of the central detector region was developed (see Figure 7). One thing which became clear as a result of the shallow crossing angle between the beams was the lack of adequate space for two independent beam pipes leading up to the inner detector region. In order to simplify the problem the decision was made to combine the two pipes into one vacuum flange in order to save space. It also became clear that an inadequate amount of space was reserved between the start of the detector region and the focusing quads on the hadron forward side. The superconducting bucking coil for the electrons only leaves 10 cm of longitudinal space for a cold to warm transition, a bellows to accommodate misalignment and thermal expansion and beam position monitors. This issue will be resolved and optimized in future iterations.

In addition to the crossing angle, one of the main parameters driving the size of the central beam pipe is synchrotron radiation. This radiation is produced when relativistic electrons are accelerated radially, or perpendicular to their velocity. To minimize this problem the electron dipole magnets have been located as far as possible ($> 50\,\mathrm{m}$) from the IR leaving adequate space to collimate the radiation produced. While the dipole magnets are responsible for the majority of the SR, the final strong focusing electron quadrupoles

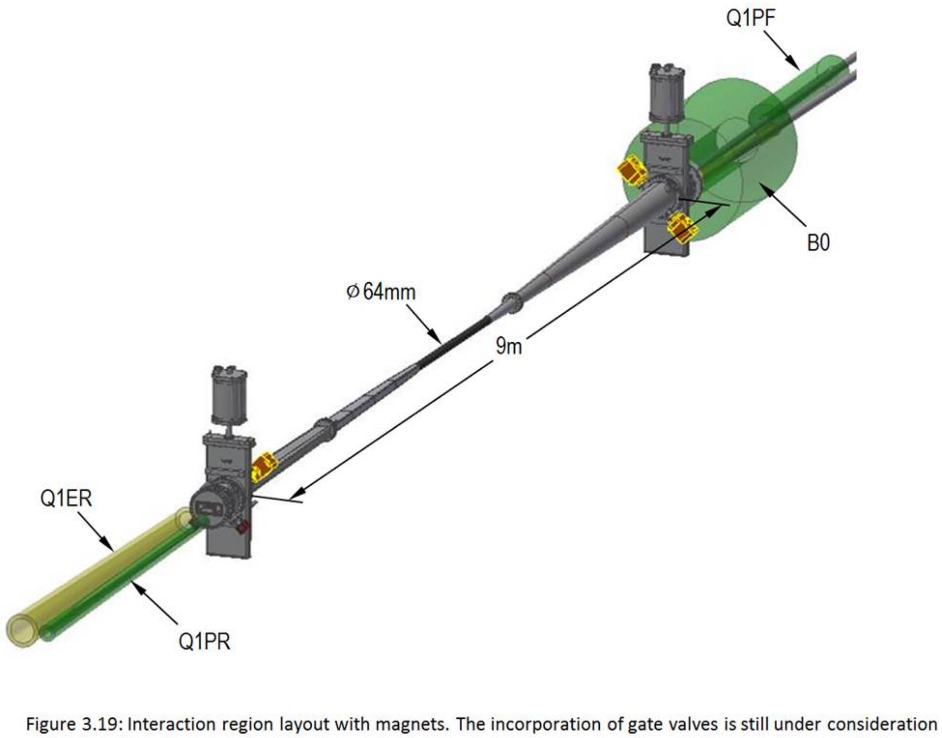

Figure 7: Interaction region layout with magnets. The incorporation of gate valves is still under consideration

located just upstream of the detector need to be taken into account. In order to study the resulting radiation (see Figure 8) a simulation study was performed using the SynRad software package developed at CERN. A stay-clear envelope was established based on the final magnet and beam parameters.

Considering the central portion of the beam pipe will be made from beryllium (see Section **??**) and taking into account its limited fabrication possibilities, a diameter of 62 mm was defined. This value provides additional clearances for mechanical and positioning tolerances. In the electron forward direction, the beam pipe will continue to increase in size to ensure the SR can travel through the IR without impinging on the chamber walls. In the hadron forward direction the beam pipe have a conical cross section in order to provide an unobstructed path to the forward spectrometer located in the B0 magnet bore. To minimize the beam impedance for the electrons, a conducting screen will be installed providing a path for the induced image currents. Once outside the central detector region the forward traveling particles will pass through a vacuum-air interface made of thin aluminum or stainless steel before entering the B0 spectrometer. Additional care will be taken with the design and position of the required chamber supports. These supports must ensure that the chamber does not encroach into the stay clear area and must also guarantee the mechanical stability of the chamber during operations and bake out. Careful consideration of the mechanical eigenfrequencies must be made to avoid large harmonic vibrations which can lead to stress and fatigue of the chamber. Where possible, support conditions will be made to keep natural frequencies $> 100\,\mathrm{Hz}$.

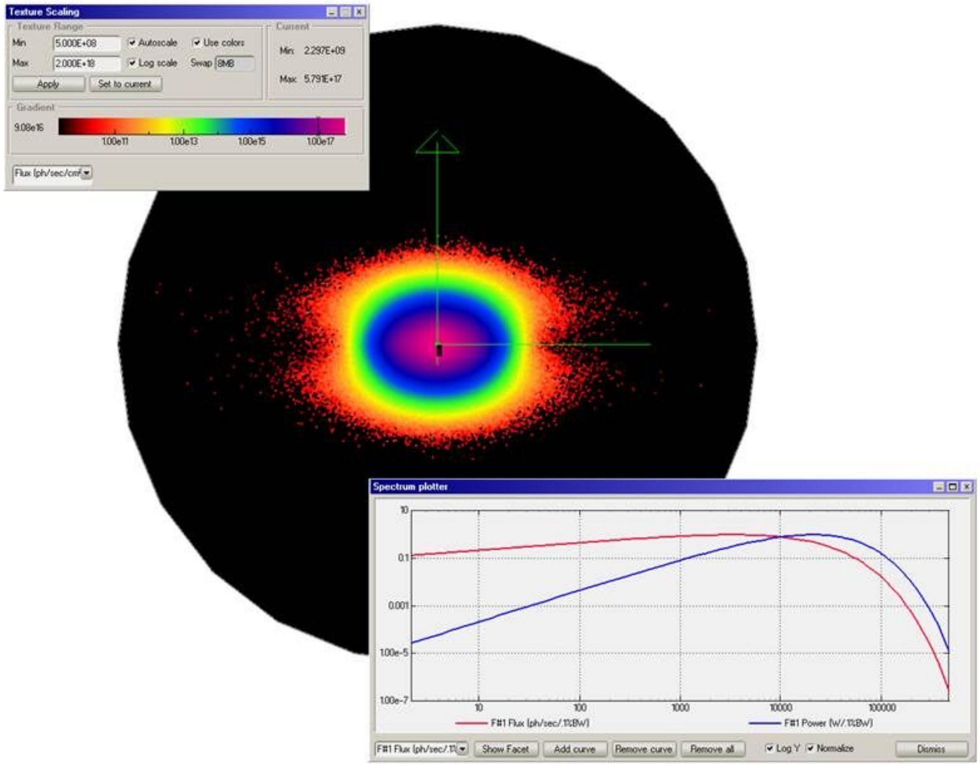

Min 5.000E+08 ☑ Autoscale ☑ Use colors

Max 2.000E+18 ☑ Log scale Swap 8MB

Current: Min: 2.297E+09 Max: 5.791E+17

Flux (ph/sec/cm²)

F#1 Flux (ph/sec/.1%BW) ☑ Log Y ☑ Normalize

Figure 8: SynRad simulation showing the resulting synchrotron radiation from the electron focusing quadrupoles Q0EF and Q1EF

1.2.2 Material Considerations

The interaction of the particles produced in the experiment and the vacuum chamber walls must be kept to a minimum. These interactions can result in an increased radiation background, reducing the sensitivity of the main detector. The transparency of a material is usually quantified through the radiation length (Ξ_0) for elastic collisions and the interaction length (l_T) for inelastic hadron collisions.

The radiation length is defined as the mean distance over which a high-energy electron loses all but $1/e$ of its energy by bremsstrahlung radiation. This property is inversely proportional to the density and atomic number of the material. The interaction length is the mean distance travelled before experiencing an inelastic nuclear interaction.

In order to reduce the background produced by these material properties, the walls of the vacuum chamber should be made as thin as possible. A limit is clearly defined by the mechanical integrity of the vacuum chamber. If the chamber is too thin, the vessel will collapse under the outside atmospheric pressure or fail to meet the tight mechanical tolerances required to stay clear of sensitive instrumentation. To compare the nuclear and mechanical performances of various materials, a figure of merit ($\Xi_0 E^{-1/3}$) has been adopted where E is Youngs modulus. The required chamber wall thickness is directly proportional to $E^{-1/3}$. Properties of several materials are listed in Table 4.

While beryllium would be the best choice it has several drawbacks including fabrication difficulties and safety concerns as well as very high cost. For these reasons, only the central portion of the IR chamber will be made from beryllium. Additional aluminum sections made from AA2219 will be electron beam welded to the center section to complete the

Table 4: Table of material properties considered for the IR vacuum pipe.

Material	ξ_0 [cm]	l_T [cm]	E [GPa]	$\Xi_0 E^{-1/3}$
Beryllium	35.3	41.8	290	2.34
Carbon fiber	27.0	40.0	200	1.58
Aluminum	8.9	28.7	70	0.37
Titanium	3.6	21.4	110	0.17

approximately 9 m long vacuum section. This particular aluminum alloy can be used at operating temperatures up to 250° C and is weldable using conventional techniques. Three separate vacuum pipes are envisioned with flange joints located at positions compatible with the central detector. The shorter pipe sections will not only simplify the fabrication, transportation and handling of the fragile chambers but facilitate NEG coating on the interior vacuum surfaces.

The magnetic properties of materials used in the interaction region will also be carefully considered. Most of the vacuum chamber components will be made of beryllium, aluminum and copper which are non-magnetic. Any stainless steel used in this region will be 316LN. This austenitic stainless steel maintains its very low magnetic permeability after welding or cold working. In general the use of stainless steel in and around this area will be avoided due to the presence of cobalt in the material and the possible formation of ^{60}Co due to neutron activation. Once formed, this radioactive isotope has a half-life of 5.3 years, severely limiting the serviceability of the area.

1.2.3 Impedance and Instabilities

From an electromagnetic standpoint, the ultimate beam pipe would be a perfectly smooth flawless conductor. This would allow the induced image currents to travel along the chamber walls without losses or forces acting back on the particle beam. In reality this is not possible and the resulting electromagnetic interactions are called wake fields. Longitudinal and transverse fields are generated when a bunch passes a sudden change in geometry or wall resistivity. Transverse fields can deflect the beam and lead to instabilities while the longitudinal wake fields lead to energy loss of the particles and localized heating of vacuum components.

In order to reduce effects related to resistivity changes, materials such as stainless steel pipes with small diameters will be copper plated. The required copper thickness depends on the shape of the beam pipe and simulation results. To minimize detrimental effects from sudden geometry changes a radial tapering guideline of 10:1 will be adhered to unless absolutely unavoidable. This means a 1 mm change in the radial distance between the particle beam and the chamber wall will occur over at least 10 mm of longitudinal space. RF shielding will be used to bridge all vacuum flange joints to prevent trapped modes and to help maintain uniform wall geometry. Even a few watts of deposited power on an uncooled vacuum surface can result in an extremely high temperature rise. Bellows which need to be installed to compensate for mechanical misalignment and provide room for thermal expansion during bake outs will also be internally shielded to avoid trapped modes. Steps inside the bellows RF shielding will be kept to a minimum. Figure 9 shows and example of a dual aperture RF shielded bellow.

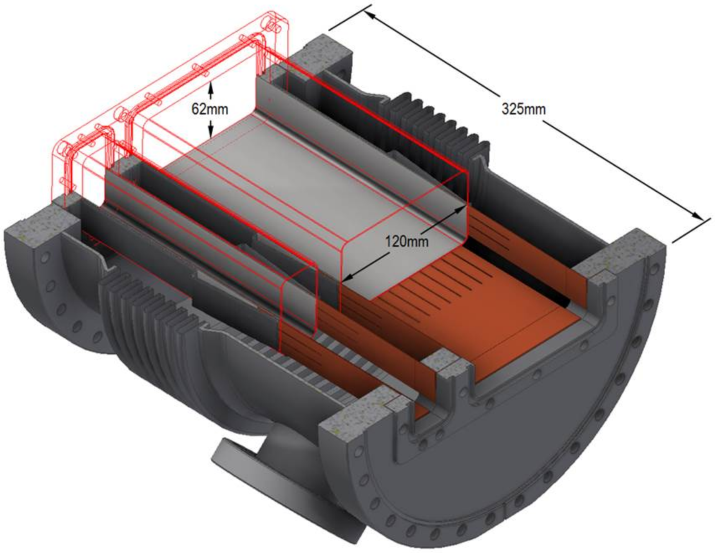

Figure 3.21: Dual aperture RF shielded bellows

Figure 9: Dual aperture RF shielded bellows

1.2.4 Vacuum Requirements

Every effort must be made to reduce the residual gas pressure in the interaction region to minimize beam-gas interactions. The first concern is related to scattering, both elastic (Coulomb) and inelastic (Bremsstrahlung). Particles in the beam which are scattered off of the remaining gas molecules can further interact with vacuum chamber walls. This in turn leads to a 'positive feedback' loop which can quickly turn catastrophic. The second concern is related to phenomena such as ion induced desorption and electron multipacting. In both of these cases charged particles, freed electrons or ionized residual gas molecules, are accelerated by the electric fields resulting from the charged particle beams. These accelerated particles can bombard the vacuum chamber walls and lead to large localized pressure rises and additional scattering. This is another self-feeding process. All of these aspects decrease the lifetime of the beam as well as the beam intensity which has a direct impact on the luminosity.

In order to eliminate the potential of unwanted contamination and ensure the lowest possible base pressure, best UHV practices will be followed from start to finish. This requires special processing of fabricated parts, careful surface treatment and minimizing the surface area exposed to vacuum. All parts will be chemically cleaned and/or vacuum baked prior to welding or assembly. After cleaning no vacuum surfaces will be touched with bare hands and all openings to vacuum surfaces will be wrapped in clean vacuum grade aluminum foil.

Given the limited space for lumped pumping as well as the need for ultra-high vacuum throughout the entire interaction region, the vacuum chamber will be coated with a non-evaporative getter (NEG) layer. This coating will be magnetron sputtered directly onto the interior surfaces of the IR vacuum chambers. NEG layers are a composition of active metals (Ti, Zr and V) which chemically pump most of the gases found in a UHV system (N_2, CO and CO_2). It also has a high diffusivity for H_2 which is the predominant gas in a baked leak tight vacuum section. The film also creates a hydrogen barrier on the interior surfaces which limits the permeation of H_2 into the system. In addition to all of these benefits the film has a low secondary electron yield which reduces the risk of electron cloud formation and being in the order of microns, adds negligible mass between the experiment and the detectors.

Incorporating NEG coating into the design has two draw backs. First is the degradation of the pumping performance after successive regenerations. Anytime the vacuum section is vented for maintenance, the NEG layer becomes completely saturated and needs to be regenerated to regain its pumping characteristics. Regenerating the layer requires dissolving the surface oxides and nitrides into the bulk material which creates a new metallic surface facing the vacuum system. Since the film is thin, it has a limited storage capacity. Some of the pumping capacity can be regained by activating at higher temperatures but the upper bound is limited by the material choices for the vacuum chambers. To increase the potential number of activations, the vacuum section will be vented with an extremely pure noble gas which is not pumped by NEGs.

Given the limited access inside the central detector region, permanently mounted heaters are envisioned to facilitate baking. Thin polyamide heaters which are made from thin metal foils sandwiched between Kapton films will be used. These heaters can be made in almost any size or shape with varying watt densities to ensure adequate heating and activation of the NEG coatings. While adding some radiation length, these are a good compromise considering the alternatives. Depending on the final design of the detector, additional insulation may be required to protect sensitive components located close to the beam pipe.

Since NEG coatings only pump active gases, ixon pumps will be installed at either side of the interaction region for residual noble gases. Ion pumps are Penning traps with crossed electrical and magnetic fields. The magnetic field increases the flight time of free electrons which ionize incoming gas molecules. These ions are then accelerated in the presence of the electric field and impact on a metallic cathode typically made of titanium or tantalum. This freshly sputtered material can physically or chemically react with gas present in the system.

1.3 Interaction Region Performance for Scientific Requirements

The physics program of an EIC and the resulting requirements for the detector and the IR have been discussed in section 1 and **??**. In order to verify that the current IR design fulfills all the requirements as summarized in Table **??**, an eRHIC general purpose detector, the auxilliary detectors, the vacuum chamber and the machine components up to the crab cavities, as shown in Figure 1, have been implemented in the EicRoot GEANT simulation framework [1]. To make the simulations as realistic as possible the beam line element 3D locations and magnetic fields are directly taken from the MADX files used for optics calculations, and their apertures precisely reflect our present understanding of how these magnets can be built in reality. The vacuum system is modeled by importing the essential part of the engineering design into GEANT.

In the following results from these simulations will be presented.

1.3.1 Realization of the Scientific Requirements for the Central Detector

Figure 2 shows clearly that the beam element free region L^* along the beam lines is ±4.5 m from the IP as required. It has been discussed in detail that in order to have the acceptance required for inclusive and semi-inclusive DIS as well as exclusive reactions it is critical to reconstruct events over a wide span in pseudo-rapidity ($-4 \leq \eta \leq 4$). Therefore the design of the vacuum system in the detector volume (see Figure 7) needs to fulfill these specifications:

- provide enough space to pass the synchrotron radiation fan through the detector
- do not extend beyond a 2^o opening angle from the interaction point.

Figure 10 shows the integration of the various detector components around the beam pipe elements in the outgoing hadron beam direction, overlaid by a deep inelastic electron-deuteron scattering event with the secondary particle tracks and hits in the TPC and the silicon trackers.

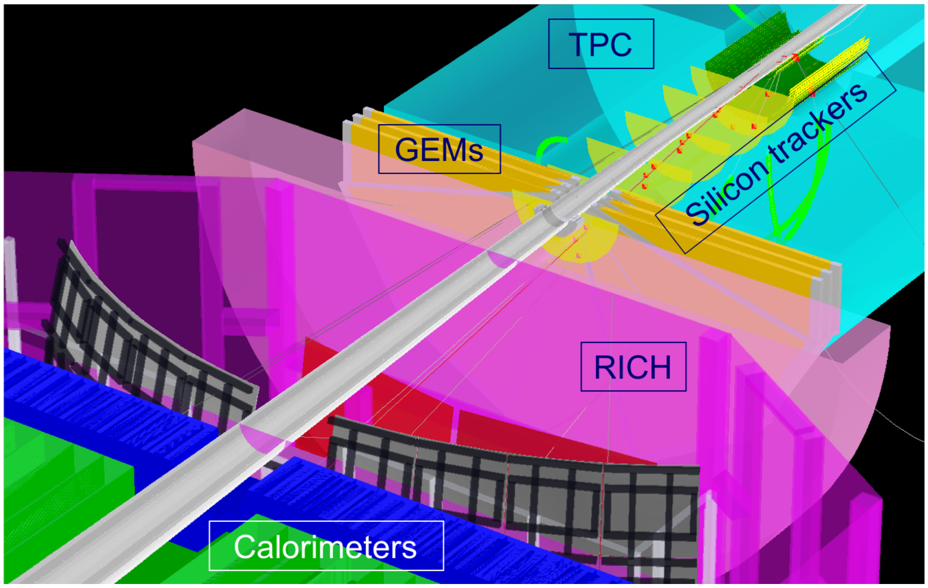

Figure 10: The integration of the beam pipe and various detector components in the outgoing hadron beam direction.

To illustrate that the tracker acceptance at large rapidities as shown above provides enough points along the particle trajectory to obtain excellent momentum resolutions up to the highest rapidities, figure 11 shows the expected momentum resolution σ_p/P as function of particle rapidity for four different particle momenta.

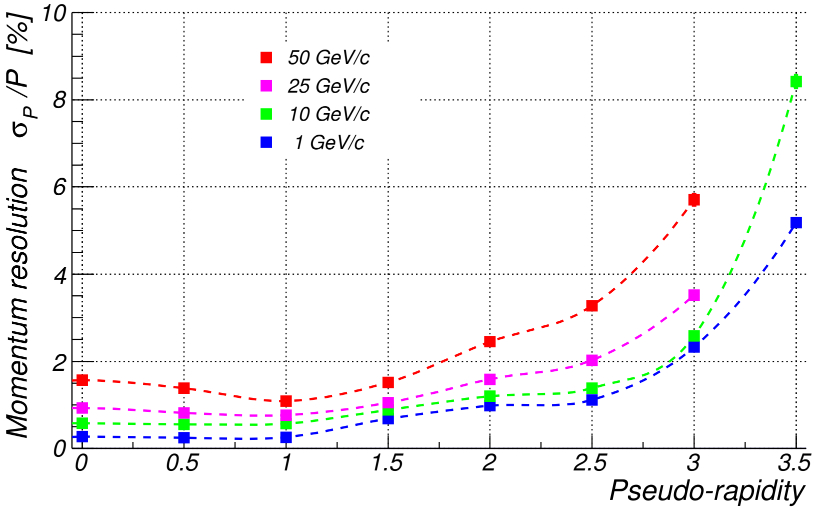

Figure 11: Momentum resolution σ_p/P as function of η for a wide range of particle momenta.

1.3.2 Realization of the Scientific Requirements for the Interaction Region

Exclusive Processes

As emphasized the detection of forward-going scattered protons from exclusive reactions as well as of neutrons from the breakup of heavy ions in incoherent and non-diffractive reactions is particularly challenging.

Electron-Proton Scattering: Extreme care has been taken to transport protons with $0.18\,\mathrm{GeV/c} < p_t < 1.3\,\mathrm{GeV/c}$ through the IR such that they can be detected as soon as they can be separated from the core of the beam. To achieve this p_t coverage over a wide range of center of mass energies a multi prong approach is required. Protons with scattering angles up to 5 mrad are detected in the Roman Pots, while the range from 7 to 20 mrad is covered by the B0 large-acceptance spectrometer (see Figure 12). The main detector in general starts seeing secondary particles above $\sim$ 30 mrad ($\eta \sim 4$), and bending power of the 3T solenoid is sufficient for momentum measurement above $\sim$ 50 mrad ($\eta \sim 3.5$ or so).

The current Roman Pot configuration has a single station with two silicon planes at $\sim$ 28 m downstream of the IP, with a relatively modest single point XY-resolution. As shown later even this very basic setup is sufficient to provide sufficient acceptance and a good momentum and scattering angle measurement.

There are several effects influencing the low p_t acceptance. We have been following the general rule of thumb that the distance between the edge of the Roman Pot silicon sensors and the core of the beam should be 10 σ in X and Y. The physical size of the 10 $\sigma_{x,y} = \sqrt{(\beta_{x,y}\epsilon_n)/\gamma}$ separation is driven by the normalized beam emittance ϵ_n and the β-function ($\beta_{x,y}$) at the location of the Roman Pots. The acceptance at large p_t is mainly constrained by the magnet apertures.

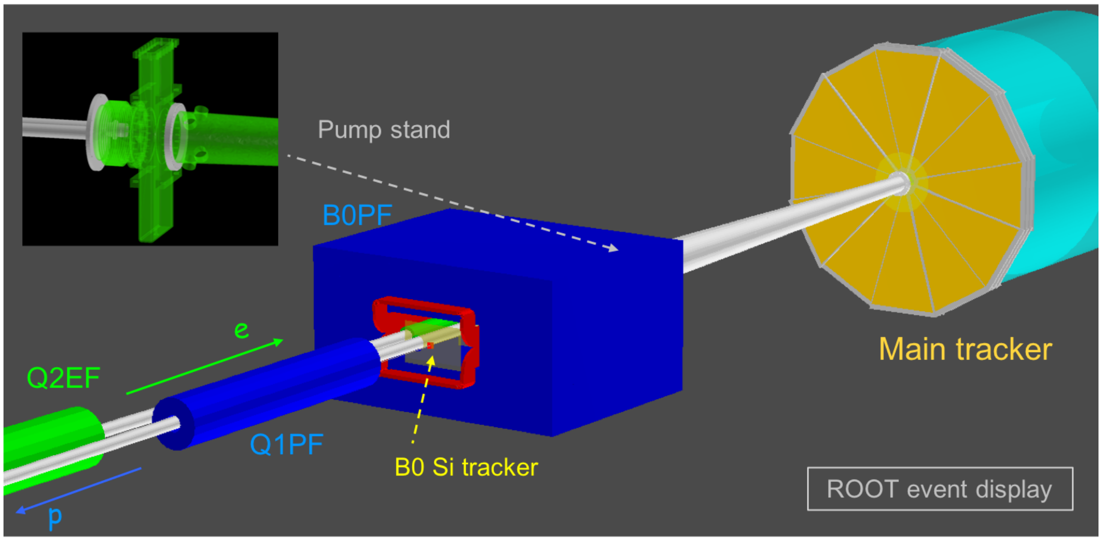

Figure 12: An EicRoot view of the B0 large-acceptance spectrometer and other equipment around it, as implemented in GEANT.

Figure 13 summarizes the p_t acceptance for three different proton beam energies, $E_p =$ 42 GeV, 100 GeV and 275 GeV for the "high beam divergence optics" (see table **??**) for eRHIC. The figures illustrate nicely the need for a multi prong detector approach to provide the full p_t acceptance over a wide range of hadrom beam energies. For $E_p = 42$ GeV the limiting factor in acceptance at high p_t is the inner dimension of the vacuum chamber and the magnet apertures. At $E_p = 100$ GeV one in general has full acceptance in p_t but there exists some "grey" (transition) area separating the forward scattered proton acceptances in the B0 spectrometer and the Roman Pots. We are currently investigating how much of this "grey" area can be filled by optimizing the layout of the outgoing 5 mrad vacuum beam pipe and/or by installation of additional Roman Pots closer to the IP. For $E_p = 275$ GeV the acceptance is mainly limited at low p_t, however this region can be partly filled by taking data with the "high acceptance beam optics" (see table **??**) for eRHIC, which is supposed to reduce the beam envelope size at the Roman Pot location and consequently relieve the 10 σ separation cut.

The p_t resolution of these forward scattered particles is of equal importance as their acceptance. Again there are several effects, which can influence the momentum resolution and need to be mitigated.

- the finite width of vertex distribution at the IP adds uncertainty in the angle determination. This uncertainty can be eliminated by determinating the vertex of the event through other tracks in the event being registered in the main detector and benefit from the excellent vertex definition by the μ-vertex detector.
- the angular divergence $\sigma_\theta = \sqrt{\epsilon_n/(\beta^*\gamma)}$ of the beam, which directly leads to a smearing of the scattering angle.
- the hadron bunch "rotation" at the IP due to the crab cavities. Crabbing implies a transverse momentum kick $p_x(z)$ to the particle bunch, with the kicking strength proportional to the longitudinal position z of particles in the bunch. Therefore at the IP particles at the "head" of the bunch will have a slightly different orientation

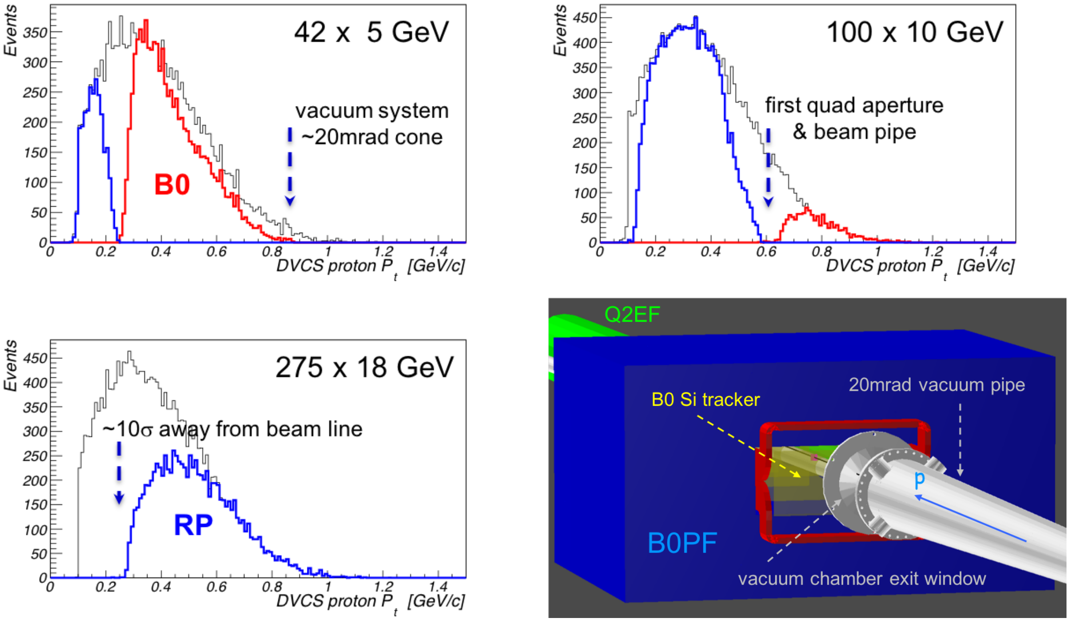

Figure 13: The p_t acceptance of forward scattered protons from DVCS (Deep-Virtual Compton Scattering) process at different combinations of beam energies. A view in the outgoing proton bema direction of the B0-spectrometer.

and/or transverse offset compared to the ones in the "tail" of the bunch, which leads to additional smearing of the apparent scattering angle. The Z-vertex determination of the event provided by the main tracker as well as high-resolution timing of the Roman Pot silicon sensors (of an order of $\sim 10\,ps$ or so) should be able to mitigate this effect to a large extent, but more studies are needed.

- the spread in the beam energy, which normally has a RMS $\sim 10^{-4}$

Currently the setup to detect the forward scattered protons is four silicon planes placed inside the bore of the 1.2 m long B0 magnet with a $\sim$ 1.3 Tesla field and a single Roman Pot station with two silicon detector planes with a relative separation of 20 cm, at $\sim$ 28 m from the IP. The silicon detectors are supposed to have 20 μm hit resolution in both X and Y. The track reconstruction is based on a Kalman filter (either with or without the vertex constraint) for the protons registered in the B0 spectrometer and a matrix transport method (with the realistic beam envelope size at the IP) for the protons registered in the Roman Pots. Under relatively conservative assumptions one obtains $\sim$ 15 MeV/c p_t resolution for the protons measured in the B0 spectrometer and $\sim$ 20 MeV/c (10 MeV/c) for protons measured in the Roman Pots in the horizontal (vertical) plane. The effect of the beam angular divergence still needs to be fully investigated.

Electron-Nucleus Scattering: As discussed in detail earlier the only possible way to tag exclusive lepton-nucleus events for heavy nuclei is to veto the nuclear break up. Figure **??** shows the break-up neutron momentum vs. scattering angle in the laboratory frame for different beam energies. For this one needs to transport neutrons within a cone of 4 mrad to 6 mrad, depending on the beam energy, through the IR to a Zero-Degree

Calorimeter (ZDC). The ZDC is placed right in front of the B2APF magnet at ~ 30 m from the IP. Figure 14 (left) shows the layout of the beam element towards the ZDC. The picture illustrates that currently neutrons are not really well centered at the $60 \times 60 cm^2$ ZDC front surface. This will be changed in the next iteration by either wrapping the ZDC around the beam pipe in a similar way to ZEUS FNC or (as indicated already in section 1.1) by moving the B1PF dipole closer to the IP for an earlier separation of neutrons from the hadron beam core. Preliminary estimates show that both options provide sufficient containment of the hadronic shower for the whole ZDC angular acceptance of $0 \div 4$ mrad.

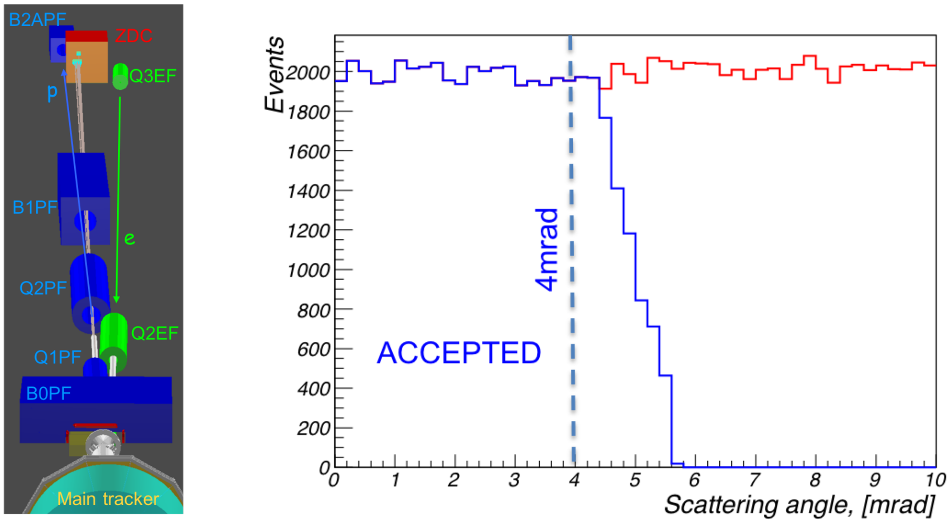

Figure 14: A view along the beam elements towards the Zero Degree Calorimeter (left). The acceptance for neutrons from nuclear break-up (right). For simplicity the neutrons have been simulated with a flat distribution in polar scattering angle.

Figure 14 (right) shows the resulting acceptance for neutrons from nuclear break-up. The required angular acceptance of ±4 mrad has been achieved and even extended beyond that (blue line) by careful consideration of machine beam line element apertures.

Electron-Nucleus Scattering:
The physics program of an EIC requires (un)polarized proton and neutron collisions to allow for a full flavor separation of (un)polarized parton distribution functions. As polarized neutron beams are not feasible, (un)polarized ^{3}He and deuteron beams are used for these purposes. To ensure the scattering really occurred on the neutron the spectator proton(s) need to be detected. Figure **??** shows the correlation of momentum and scattering angle for the spectator protons from lepton-deuteron and lepton-^{3}He scattering for two different values of $\sqrt{s}$. Figure 15 shows the angular and momentum acceptance for spectator protons from inelastic electron-deuteron collisions as simulated with the MC generator DPMJET [2] and passed through the complete simulation of the interaction region. For both hadron beam energies E_p 42 GeV and 100 GeV full acceptance is achieved. The response for spectator protons from ^{3}He will be basically identical as the angular momentum distribution for spectator protons is practically the same and their rigidity is closer to the beam rigidity.

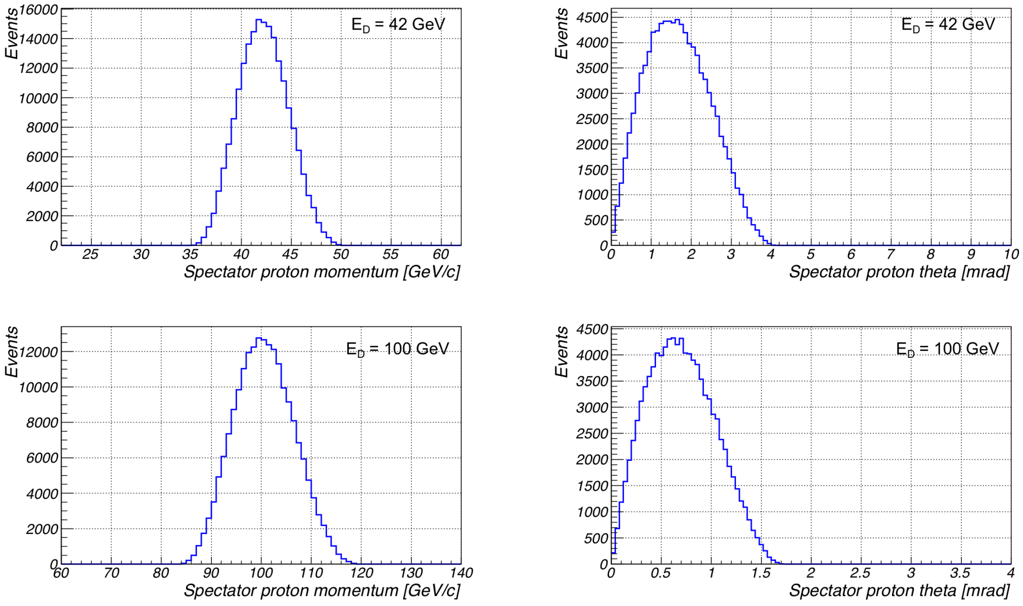

Figure 15: The momentum and angular acceptance for spectator protons from inelastic electron-deuteron collisions for hadron beam energies E_D of 42 GeV (top) and 100 GeV (bottom) per nucleon, respectively.

Inclusive Processes:

There are many physics topics beyond the ones discussed in the EIC White Paper [3], which benefit from tagging the scattered lepton at Q^2 values significantly below $1\,\mathrm{GeV}^2$. Scattered leptons with a $Q^2 < 0.5\,\mathrm{GeV}^2$ cannot be detected in the main detector. Therefore, similar to the HERA collider detectors, a special low-Q^2 tagger is needed. An electromagnetic calorimeter with a number of silicon tracking planes in front of it needs to be integrated into the IR design to detect the scattered leptons with low Q^2. Figure 16 gives a view along the outgoing electron beam from the main detector towards the low Q^2-tagger. As shown in fig. 2 (left) the magnet apertures need to be large enough to pass the synchrotron radiation fan as well as scattered leptons with low Q^2.

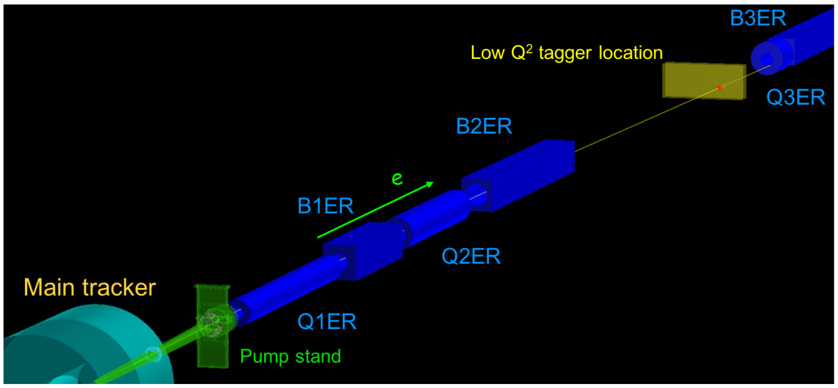

Figure 16: A view along the outgoing electron beam from the main detector towards the low-Q^2 tagger.

Figure 17 shows the Q^2 acceptance of the low Q^2-tagger for the highest eRHIC electron-proton energies of 18 × 275 GeV. The black histogram are all generated PYTHIA events. The green one shows the same events after taking the aperatures of the quadrupoles and dipoles into account. If one also considers that (similar to the Roman Pots) one needs to keep a 10σ clearance between the beam central trajectory and the detector one obtains the Q^2 acceptance as shown in the blue histogram. Currently the magnet apertures limit the acceptance at high Q^2 to ~ 0.001 $(GeV/c)^2$ and at low Q^2 the acceptance is constrained by the 10σ clearance requirement.

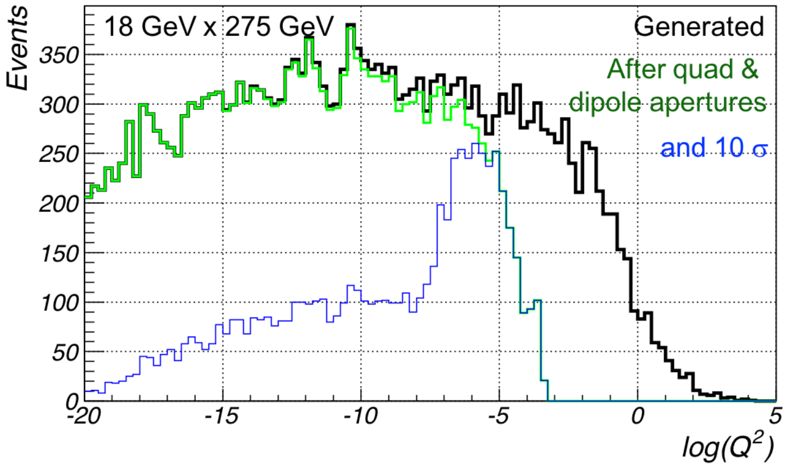

Figure 17: The Q^2 acceptance of the low Q^2-tagger after accounting for the apertures of the quadrupoles and dipoles (green histogram) as well as that of a 10σ distance separation, which needs to be kept between the low Q^2-tagger tracker and the core of the lepton beam (blue histogram). The spectra are for $e+p$ collisions at 18 × 275 GeV.

The preliminary conclusion of these physics simulation studies is that the current IR design fulfills most of the requirements summarized in table **??**. Several potential improvements to the design are identified already, which will extend the eRHIC physics reach even further.

1.4 eRHIC Crab Cavity Requirement and Specifications

1.4.1 eRHIC Crab Cavity Introduction

The concept of crab crossing as a countermeasure to the geometric reduction in luminosity caused by the crossing angle in colliders was introduced in 1988 [4]. A crab cavity imparts a transverse momentum kick $p_x(z)$ to the particle bunch, with the kicking strength proportional to the longitudinal position z of the particle. At the right phase, the bunch arrives at the cavity with its center particle receiving an accumulative zero deflection. The transverse momentum kick can be expressed as

$$p_x(z) = \frac{eE_0}{\omega}\sin(kz)\sin\left(\frac{kL}{2}\right) \approx \frac{eE_0 z}{c}\sin\left(\frac{kL}{2}\right) \tag{2}$$

where E_0 is the amplitude of the electric field acting on the bunch, ω and k are the angular frequency and the wave number of the crab cavity, respectively, and L is the bunch length. The longitudinal coordinate z is referencing to the center of the bunch, where $z = 0$. A transverse oscillation translates the longitudinally dependent kick p_x to a transverse offset x_{IP} at the interaction point (IP), which gives

$$x_{\mathrm{IP}} = R_{12}\frac{p_x c}{E_b} = \sqrt{\beta_{\mathrm{crab}}\beta^*}\frac{eE_0 z\sin\left(\frac{kL}{2}\right)}{E_b} \tag{3}$$

where R_{12} is the element of the transverse transfer matrix from the crab cavity to the IP; β_{crab} and β^* are the β-functions at the crab cavity and the IP.

At the correct cavity voltage, the transverse offset will cancel the crossing angle in the optics and restore the head-on collision. The requirement to the transverse offset can be exchanged with the crossing angle as

$$\theta_c = \frac{2x_{\mathrm{IP}}(z)}{z} = \sqrt{\beta_{\mathrm{crab}}\beta^*}\frac{2eE_0\sin\left(\frac{kL}{2}\right)}{E_b} \tag{4}$$

For a beam energy E_b, the correct voltage is

$$V = \frac{cE_b\theta_c}{2e\omega\sqrt{\beta_{\mathrm{crab}}\beta^*}}; \tag{5}$$

here we assume that the phase advance between the crab cavity location and the IP is exactly $\frac{\pi}{2}$.

1.4.2 eRHIC Crab Cavity Requirement and Specifications

The eRHIC crossing angle is in the horizontal plane. Based on the bunch length and feasibility of fabrication, the crab cavity frequency of the eRHIC ion beam is chosen to be 337.8 MHz, which is the 12th harmonic of the bunch frequency. To minimize the design risk and single cavity fabrication cost, the electron beam will share the same crab cavity design with the ions. With shorter bunch length and lower energy, the requirements to the crab cavity system for the electron beam are below 50% of the requirements from the ion beam. Thus, the crab cavity system development focused on the ion beam requirement, which would fulfill both beams. Table 5 shows the crab cavity related lattice parameters and the calculated voltage requirement for each scenario. The table also compares the eRHIC crab cavity with the existing crab cavities at KEKB and Hi-Lumi LHC [5, 6, 7]. The frequency

Table 5: Comparison of crab cavity parameters.

	KEKB		Hi-Lumi LHC	eRHIC no cooling		eRHIC with cooling	
Parameter	LER	HER	both	ion	electron	ion	electron
Full crossing angle [mrad]	22	22	0.59	22	22	22	22
Energy [GeV]	3.5	8	7000	250	18	250	18
RMS bunch length [cm]	0.7	0.6	7	7	2.3	4	1.7
Frequency [MHz]	509	509	400	338	338	338	338
Wave number [m^{-1}]	10.6679	10.6679	8.3834	7.0799	7.0799	7.0799	7.0799
Wave length [m]	0.5890	0.5890	0.7495	0.8875	0.8875	0.8875	0.8875
Scheme	global		local	local	local	local	local
6σ of wavelength [%]	0.0713	0.0611	0.5604	0.4733	0.1555	0.2704	0.1149
β at IP [m]	1.2	1.2	0.15	0.92	0.56	0.67	0.23
β at crab cavity [m]	51	122	2616	1600	150	1600	150
Horizontal beam size [μm]	110	110	7	119	119	77	77
Piwinski angle [rad]	0.70	0.60	2.95	6.47	2.13	5.71	2.43
Voltage [MV]	0.92	1.36	12.43	10.12	3.05	11.86	4.76

difference between the Hi-Lumi LHC and eRHIC crab cavities is below 16%, with the same operational deflecting voltage. Therefore, the experience from the LHC crab cavity program can directly benefit eRHIC in most aspects.

The location of the crab cavity is chosen with consideration of minimizing the voltage, i.e. at a high-β location. However, the dispersion functions at the crab cavity locations are non-zero for both rings, which generates linear and non-linear instabilities with beam-beam interaction. Analysis of the detailed beam dynamics with crab crossing is discussed in Section **??**.

The spatial allowance for crab cavity system installation is limited by the distance between the electron and the ion beam lines in the horizontal direction, and the local structures in the vertical plane, e.g. cable trays, cryogenic transfer lines, and the tunnel floor. In the meantime, the IR is highly utilized region for various species of magnets and instrumentation devices, along with their auxilaries. In the eRHIC lattice, the crab cavity systems are given about 7 meters of longitudinal space to provide a deflecting voltage of 11.86 MV. Figure 18 shows the ion ring lattice in the interaction region (IR), with the electron storage ring along the $x = 0$ direction in the same horizontal plane as the ion beam line. The location of the crab cavity cryomodule is about 50 m on both sides to the interaction point (IP), where the distance between the centers of the two beam lines is ~ 1.1 m. These limits needed to be well considered at the beginning of the cavity, coupler, helium vessel, tuner and cryomodule development to avoid any significant changes in the future.

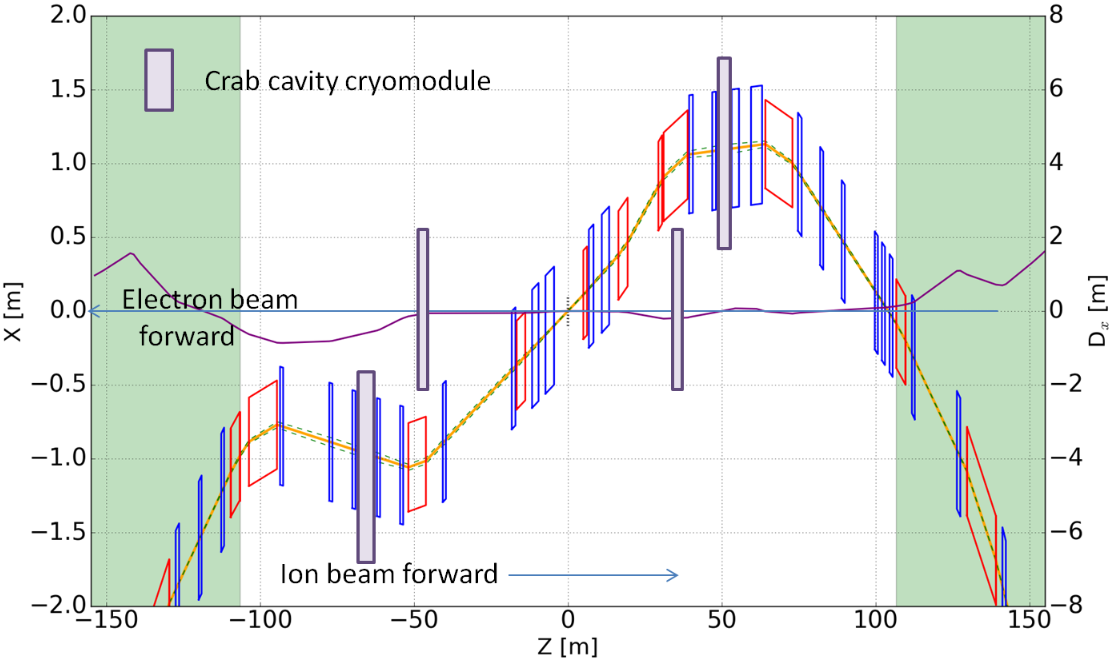

Figure 18: Schematic drawing of the local configuration of all beam lines near the crab cavity installation region, top view.

1.5 Impedance Modeling

The main parameters to estimate the collective effects are given in Table 6. To estimate the instability thresholds, an approximation to the wake-potential for a 0.3 mm bunch length, much shorter than the 19 mm length of the unperturbed circulating bunch is used for beam dynamics simulations in the SPACE particle tracking code [8].

Table 6: Parameter for threshold calculation

Energy	E [GeV]	10
Revolution Period	T_0 [μs]	12.79
Momentum Compaction	α	1.45×10^{-3}
Energy Loss	U [keV]	9100
RF Voltage	V [MV]	41
Synchrotron tune	ν_s	0.0815
Damping Time	τ_x, τ_s [ms]	70, 35
Energy Spread	σ_δ	5.5×10^{-4}
Bunch Length	σ_s [mm]	19

1.5.1 IR Chamber

The preliminary geometry of the interaction region (IR) chamber is presented in Fig. 19. This IR chamber has a complex geometry; its cross-section changes along the z-axis. The cross-sectional top view of the IR chamber is shown in Fig. 20 (upstream) and Fig. 21 (downstream). The sectional view of the upstream IR chamber with electron beam pipe 50 mm × 50 mm is shown in Fig. 22.

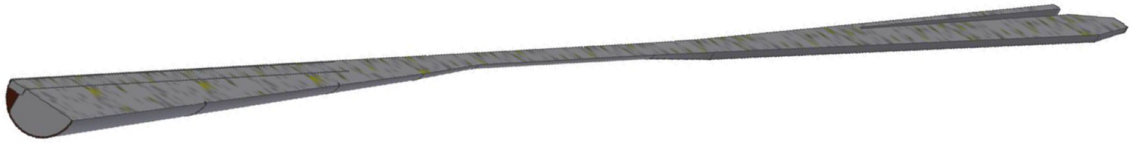

Figure 19: 3D rendered image of the interaction region chamber

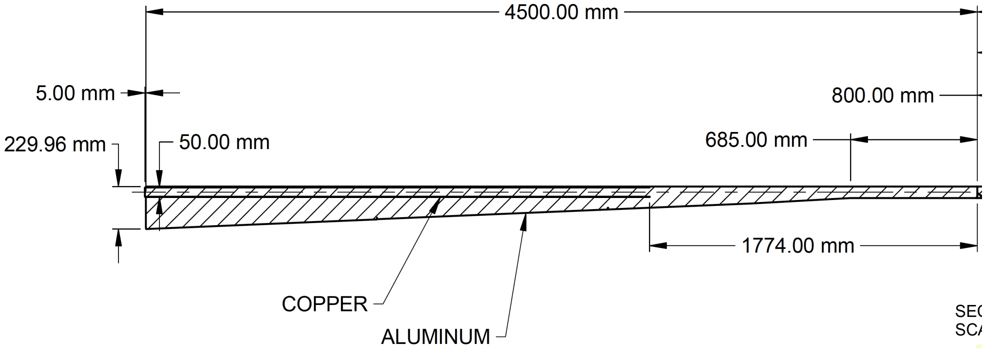

Figure 20: Cross-sectional top view of the upstream IR chamber.

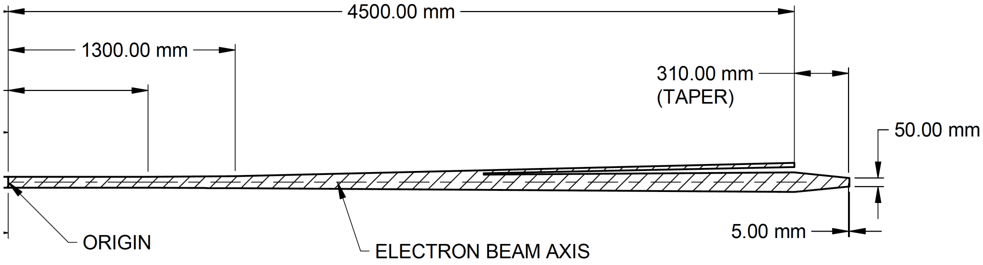

Figure 21: Cross-sectional top view of the downstream IR chamber

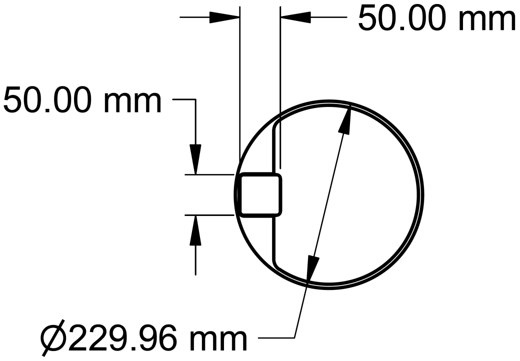

Figure 22: Section view of the upstream IR chamber entrance. The electron beam chamber has a square profile with a full aperture 50 mm × 50 mm.

The impedance analysis has been performed using the GdfidL code [9]. The results of the numerical simulations are shown in Fig. 23 and Fig. 24. Using the machine parameters and the simulated results we can estimate the heat load due to multiple passes of the bunch train through the structure. The power loss is

$$P_{\text{loss}} = \kappa_{\text{loss}} I_{\text{av}}^2 T_0 / M, \tag{6}$$

where M is the number of bunches, T_0 is the revolution period, and I_{av} is the average current. Using the simulated geometric loss factor $k_{\text{loss}} = 0.2\,\text{V/pC}$, the power loss is $P_{\text{loss}} = 22.6\,\text{kW}$ for $M = 660$ bunches and $I_{\text{av}} = 2.48\,\text{A}$. The geometry has step transitions and needs to be optimized from the impedance point of view. The level of the heat-load has to be reduced. Several optimization steps are required.

1.5.2 Longitudinal Impedance Model

By passing through the vacuum chamber, the electron beam generates electromagnetic fields, which can affect the beam stability at much lower beam intensity than the design parameters. Hence, it is important to determine the impedance/wakepotential of all vacuum components distributed around the ring that are experienced by the electron beam. The preliminary vacuum components list is presented in Table 7. The geometric dimensions and the surface resistivity of many vacuum components are not known yet. As a first attempt, we apply the wakepotential/impedance simulated for the NSLS-II vacuum components with eRHIC main lattice parameters for the instability thresholds estimation. The geometric impedance due to cross-section changes in the vacuum components has been calculated by the GdfidL code. Based on the status of simulations, the vacuum components are

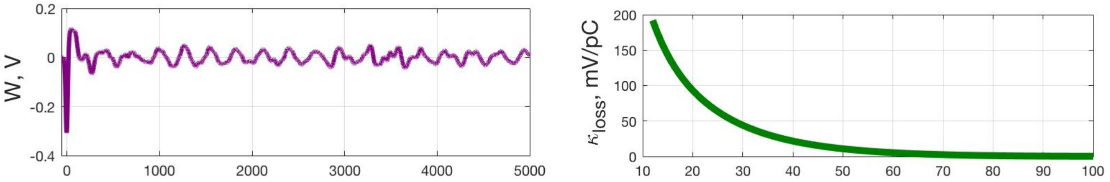

Figure 23: Numerically simulated data for the IR chamber. Left: Longitudinal wakepotential $W_{||}(s)$ simulated for a $\sigma_s = 12\,\text{mm}$. Right: Loss factor dependence of the bunch length σ_s

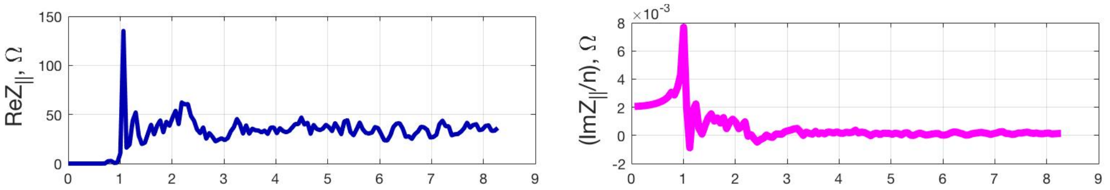

Figure 24: Left: Real part of the longitudinal impedance. Right: Imaginary part of the longitudinal impedance divided by $n = \omega/\omega_0$, where $\omega_0 = 2\pi \times 78.186\,\text{kHz}$

marked as "NSLS-II" or the "eRHIC", based on the applied wakepotential. With more update in geometries and their optimization from the impedance point of view for the eRHIC project, the NSLS-II wakepotential/impedance data will be replaced and the new wakepotential/impedance data will be used to generate the total impedance budget for particle tracking simulations and analytical evaluation. The contribution of the resistive wall to the total impedance is calculated separately by applying the analytical approach derived by Bane and Sands [10],

$$W_{||}(\tau) = \frac{r_e mc^2 N_e}{2b\sqrt{2\mu_r Z_0 \sigma_{\text{con}}}} i \left|\frac{\tau}{\sigma_s}\right|^{3/2} e^{-\tau^2/4\sigma_s^2} \times \left[I_{1/4}\left(\frac{\tau^2}{4\sigma_s^2}\right) - I_{-3/4}\left(\frac{\tau^2}{4\sigma_s^2}\right) \right. \tag{7}$$

$$\left. -\text{sgn}(\tau) I_{-1/4}\left(\frac{\tau^2}{4\sigma_s^2}\right) + \text{sgn}(\tau) I_{3/4}\left(\frac{\tau^2}{4\sigma_s^2}\right) \right], \tag{8}$$

where b is the vacuum chamber radius, $Z_0 = 120\pi$ is the impedance of free space, σ_s is the electrical conductivity and μ_r is the relative permeability of the chamber surface. As a preliminary estimate for the resistive wall surface, six 257 m long arc sections made of copper with a radius of 20 mm and twelve 123 m long copper straight sections with radius of 20 mm are taken into account.

The total longitudinal wakepotential as a sum of the short-range geometric and resistive-wall longitudinal wakepotentials is shown in Fig. 25. The frequency spectrum of the real part of the total longitudinal impedance is presented in Fig. 26 up to 350 GHz.

The computed total longitudinal wakepotential $W_{||,\text{tot}}$ applied as an input file for the SPACE particle tracking code using the parameters for beam dynamics simulations presented is in Table 6. Numerical simulations are done using 30 million macro-particles and 800 grid points in order to accurately determine the first microwave instability threshold and to characterize the microwave dynamics above it. The energy spread of the unperturbed Gaussian bunch at low current is estimated at $\sigma_\delta = 5.65 \times 10^{-4}$. The first microwave instability threshold is observed at $I_{\text{th}} = 4.5\,\text{mA}$ (Fig. 27), which is above the single bunch current of 3.8 mA. The bunch lengthening effect due to potential-well distortion (Fig. 27)

Table 7: List of the vacuum components contributing to the total impedance of the electron storage ring.

Object	Abbreviation	Number of components	Project
Bellows	BLW	380	NSLS-II
LA BPM	LABPM	494	NSLS-II
Stripline	SL	18	NSLS-II
Gate Valve	GV	45	NSLS-II
Flange Absorber	FABS	200	NSLS-II
RF Cavity	CAV	23	NSLS-II
RF Tapered Transition	TPRDRF	—	NSLS-II
IR Chamber	IRCHM	1	eRHIC

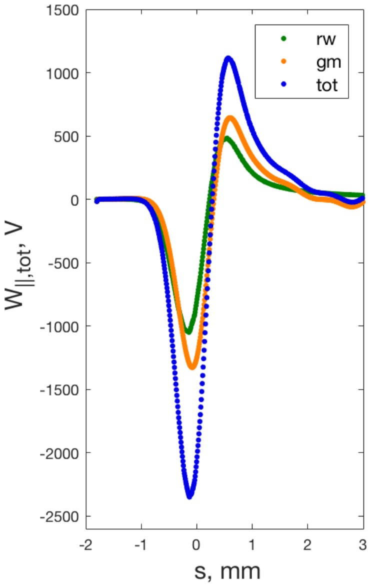

Figure 25: Longitudinal short-range wakepotential calculated for a bunch length of $\sigma_s = 0.3$ mm. The total longitudinal wakepotential of the eRHIC project (blue trace) is a sum of the resistive wall contribution (green trace) calculated analytically (Eq. (8)) and the geometric wakepotentials (orange trace)

is small enough up to 4 mA for the applied total longitudinal wakepotential.

1.6 Betatron Tune Dependence on Electron Beam Intensity

For the octagonal shape of the dipole vacuum chamber with a half-aperture $b = 20mm$ and dipole magnet half-gap $d = 26mm$, the multi-bunch current dependent betatron tune shift induced by the quadrupole impedance of the dipole magnets at frequency $\omega \to 0$ is given by

$$\Delta\nu_{x,y} = \frac{I_{\text{av}}L}{4\pi E/e}\beta_{x,y}\text{Im}Z_{Q_{x,y}}(0), \tag{9}$$

where $L = 192 \times 6.064$ m is the total length of the dipole magnets, $I_{\text{av}} = 2.48$ A is the average current, $\beta_x = 17$ m and $\beta_y = 18$ m are the local horizontal and vertical average

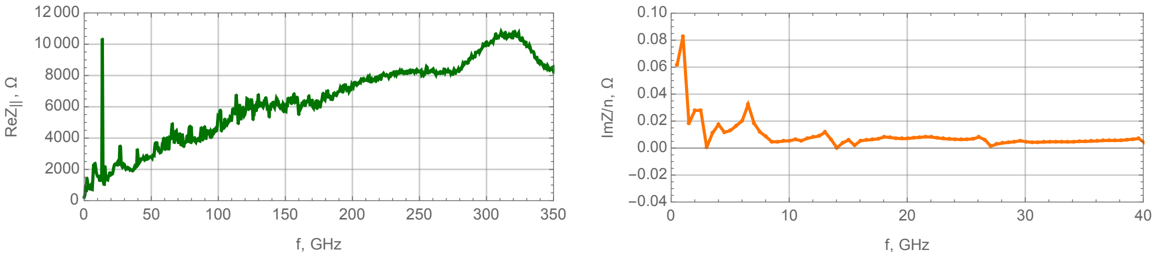

Figure 26: left: Real part of the longitudinal impedance. Right: Imaginary part of the longitudinal impedance divided by $n = \omega/\omega_0$, where $\omega_0 = 2\pi \times 78.186\,\mathrm{kHz}$

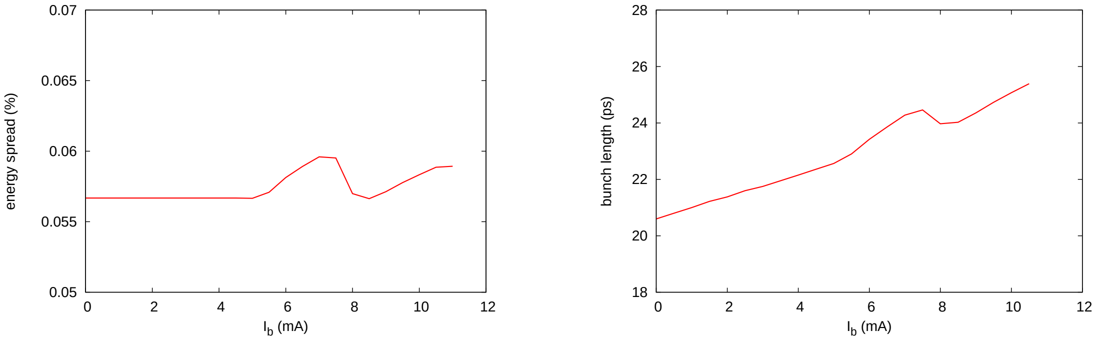

Figure 27: Top: Energy spread as a function of single bunch current. Bottom: Bunch lengthening dependence on the single-bunch current

β-functions, $E = 10\,\mathrm{GeV}$ is the electron beam energy and $\mathrm{Im}Z_{Q_{x,y}}$ is the imaginary part of the quadrupole impedance. For the dipole magnets, the quadrupole impedance $\mathrm{Im}Z_{Q_{x,y}}$ is analytically approximated by a multi-parallel plates model [11]

$$ImZ_{Q_{x,y}}(0) = \pm\frac{\pi^2}{12cb^2}\left(1 + 2\frac{b^2}{d^2}f(\eta)\right), \tag{10}$$

where

$$f(\eta) = \frac{6}{\pi^2}Li_2(\eta), \tag{11}$$

and

$$\eta = \frac{\mu_r - 1}{\mu_r + 1}. \tag{12}$$

With relative permeability $\mu_r \to 0$ (perfect magnets) $f(\eta) = 1$. We notice that Eq. (10) differs by a factor of 2 from the formula for the resistive wall impedance derived by Chao, Heifets and Zotter in Ref. [12] using the well known Laslett coefficients [13]. The validity of

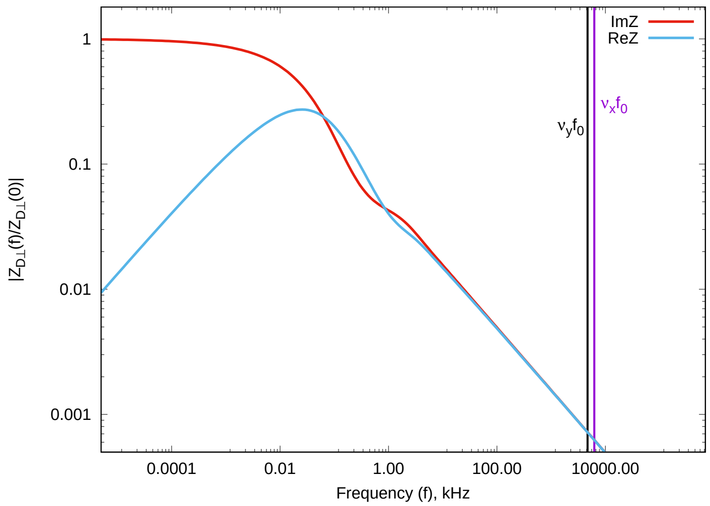

Figure 28: Absolute value of the ratio of the transverse dipole impedance to the quadrupole impedance evaluated at zero frequency. Here $\perp$ is either x or y. The dipole and quadrupole impedances are related as follows: $Z_{D_x}(f) = -Z_{Q_x}(f)$, $Z_{D_y}(f) = Z_{Q_y}(f)$. The dipole impedance is obtained numerically by the standard field matching technique as applied in [11], with dipole chamber conductivity $\sigma_{\mathrm{Cu}} = 54\,\mathrm{S/m}$ and thickness $t = 3\,\mathrm{mm}$. The dipole impedance, evaluated at $f = \nu_\perp f_0$ with parameters $\nu_x = 0.08$, $\nu_y = 0.06$ and $f_0 = 78196.5\,\mathrm{kHz}$ is negligible with respect to the quadrupole impedance evaluated at $f = 0$, thus justifying the validity of Eq.(9).

Eq.(9), where the only contribution to the betatron tune shift is given by the quadrupole impedance evaluated at zero frequency, is justified by the fact that the first contribution from the dipole impedance, which is given by the impedance evaluated at $\nu_\perp f_0$, where $\nu_\perp$ is the fractional betatron tune and $\perp = x$ or y, is negligible, as shown in Fig.28 for the nominal fractional betatron tunes $\nu_x = 0.08$ and $\nu_y = 0.06$.

The calculated betatron tunes ν_x and ν_y as a function of average current I_{av} are presented in Fig. 28. At the nominal $I_{\mathrm{av}} = 2.48\,\mathrm{A}$, the estimated tune shifts $\Delta\nu_x = 0.05$ and $\Delta\nu_y = -.05$ might affect the lattice optimization to mitigate the beam-beam interaction [14]. To eliminate the effect of the quadrupole impedance on the multi-bunch tune shift dependence vs. the average current, the dipole vacuum chamber should be considered with a circular profile.

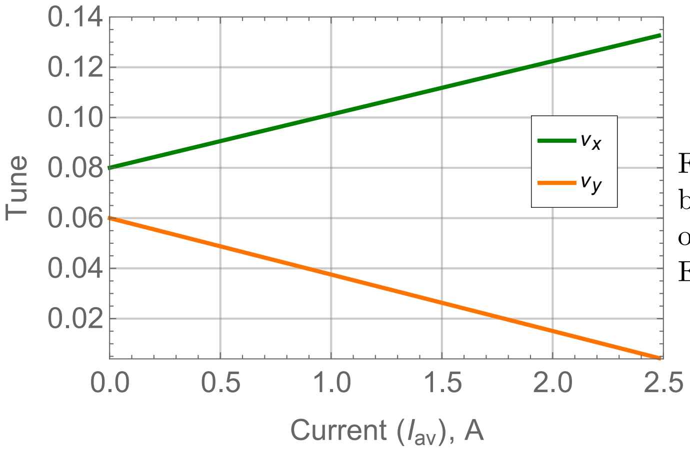

Figure 29: Horizontal and vertical betatron tune shifts as a function of average current estimated using Eq.(9).

1.7 IR Synchrotron Radiation Analysis

The IR crossing angle scheme avoids the necessity of separator dipoles in or near the detector which would generate a wide fan of hard synchrotron radiation photons. However, the nearby low-β quadrupoles generate a synchrotron radiation cone that can be equally harmful for the detector if not handled appropriately.

In contrast to the homogeneous fan produced by dipole magnets, the photon cone generated by quadrupoles consists of a huge number of weak photons in its center, and a comparatively small number of very high energy photons at increasing distances from the center that stem from electrons in the transverse tails of the beam distribution that have experienced strong magnetic fields at large amplitudes in these low-β quadrupoles. Additionally, since the beam-beam interaction tends to result in an over-population of the transverse electron beam tails, especially in the vertical plane, the number of hard photons produced in the quadrupoles by large-amplitude electrons can be significantly higher than for a pure Gaussian distribution. All these factors therefore have to be taken into account when evaluating the synchrotron radiation background in the detector, and designing a masking scheme.

The nonlinear nature of the beam-beam interaction leads to the formation of non-Gaussian tails with an enhanced electron density. As Figure 30 shows, the colliding electron beam requires about 50 percent larger apertures than without beam-beam interactions. Magnet apertures have to be large enough for these tails to pass through in order to provide beam lifetimes on the order of at least several hours. Since the synchrotron radiation masks have to provide sufficient aperture for the circulating electron beam as well these effects have to be taken into account in their layout.

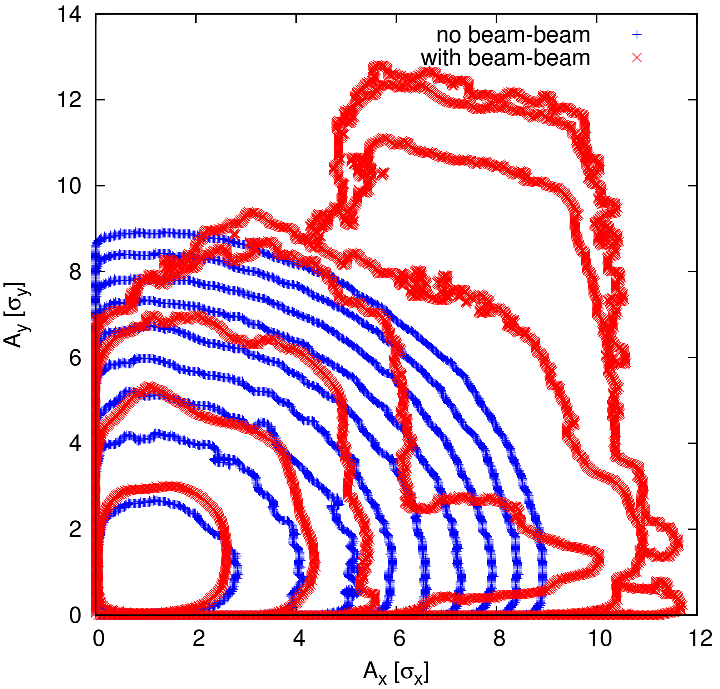

Figure 30: Transverse electron density distribution with (red) and without (blue) beam-beam interaction. The contour lines are spaced by a factor 10.

The eRHIC Physics program requires a machine element free region of ±4.5 m around

Table 8: Electron IR magnet parameters on the upstream side of the detector, for the highest design energy of 18 GeV

name	s_i [m]	l [m]	IR [cm]	B [T]	g [T/m]
Q0EF	5.00	1.2	2.2	0.309	-14.1
Q1EF	8.74	1.72	4.85	0.282	6.0

the IP for the installation of the central detector. As a consequence, any synchrotron radiation mask that gets hit by direct radiation can only be installed at least 4.5 m from the IP. The aperture of those masks has to be sufficiently large to ensure beam lifetimes on the order of several hours. With aperture radii corresponding to 10 transverse RMS beam sizes of the Gaussian, non-colliding beam, we can accommodate non-Gaussian tails that correspond to a 6σ aperture restriction. Based on this we expect beam lifetimes of the order of 25 hours [15].

The first focusing element (quadrupole Q1) starts at a distance of 5.0 m from the IP. In order to reduce the peak magnetic fields encountered by electrons in the transverse tails, this magnet as well as the following quadrupole Q2 are comparatively long; the length is limited by the requirement to fit in-between focusing elements in the hadron beam line in an interleaved fashion [16]. Table 8 lists the design parameters of the last four quadrupoles upstream of the IP.

To shield the detector from direct hits by synchrotron radiation photons we assume a mask at $s = 4.5$ m upstream of the IP, just outside the central detector. This mask minimizes the width and height of the fan generated by upstream quadrupoles through the detector. A second mask is located further upstream; the purpose of this mask is to reduce the heat load on the 4.5 m mask by capturing photons that originate further upstream.

This masking scheme results in an elliptical cone of the synchrotron radiation fan through the central detector. On the incoming side, its cross section is identical to that of the mask at $s = 4.5$ m, which is determined by the 10σ beam size at that location. The radii of that upstream ellipse are 11 mm in the horizontal plane, and 10 mm vertically. At the downstream end of the central detector, the cone radii have substantially increased, to 71 mm horizontally, and 19 mm vertically. This cone determines the minimum dimensions of the detector beam pipe that ensure no background from primary photons generated by the electron beam.

In the next step, the impact of potentially backscattered photons on the detector is simulated using the code DESYNC [17].

The focusing upstream of the detector is designed such as to minimize the magnetic fields of the last two quadrupoles encountered by electrons in the transverse tails of the beam. This is accomplished by long quadrupoles Q0EF and Q1EF with a low gradient. Even at the highest beam energy of 18 GeV this results in peak fields of only 0.3 T at the 15σ design aperture of these magnets. However, since the moveable upstream mask at $s = 4.5$ m has an aperture radius of only 10σ, no electrons are present in the beam beyond this limit. Therefore, the maximum magnetic field sampled is only 2/3 of the peak field of those quadrupoles, namely $B_{\mathrm{max}} = 0.2$ T. The corresponding critical energy of the synchrotron radiation generated by the small number of electrons at the outer edges of the

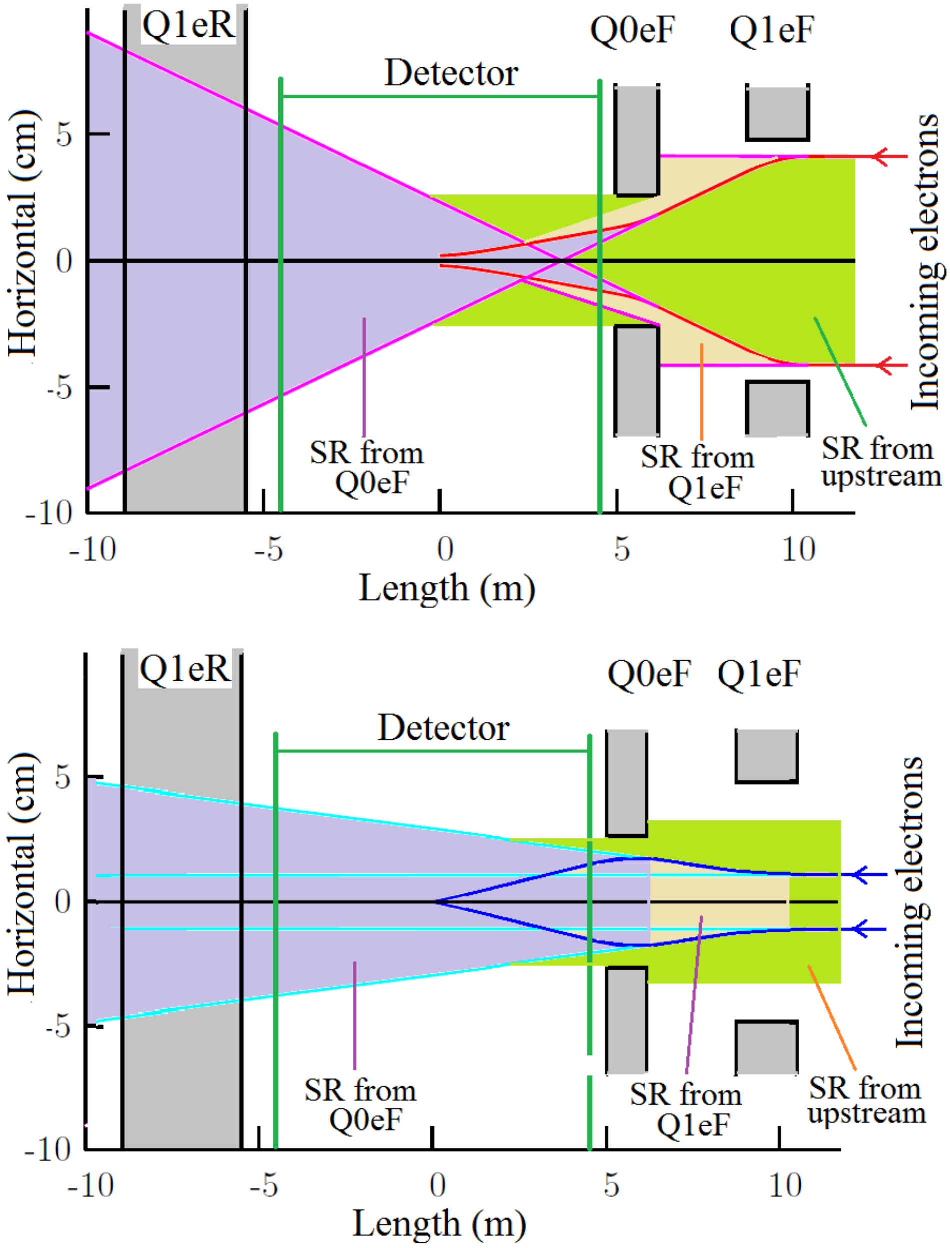

Figure 31: Synchrotron radiation fans from the low-β quadrupole doublet through the IR, top view (top) and side view (bottom).

beam is therefore reduced to

$$\begin{aligned} E_c &= \frac{3}{2}\frac{\hbar c^2 e E^2 B}{E_0^3} \\ &= 43.2\,\text{keV}, \end{aligned} \tag{13}$$

at 18 GeV, or $E_c = 13.3\,\text{keV}$ at $E = 10\,\text{GeV}$. Here $E_0 = m_e c^2$ is the electron rest energy.

Photon scattering in the IR geometry described above has been simulated with the code DESYNC [17]. Assuming a detector beam pipe that is tailored to accomodate the primary synchrotron radiation fan according to Figure 31 the radiation load outside the

1 mm thick beryllium detector pipe reaches a maximum of 2.2 rad/hour at 18 GeV in the 1 m long section right after the mask, and less than a μrad/hour everywhere else throughout the central detector. At a beam energy of 10 GeV the maximum reduces by 2-3 orders of magnitude.

While these radiation levels are likely acceptable more detailed simulations including the actual eRHIC detector are required. These simulations are beyond the capabilities of DESYNC and will therefore be carried out using a simulation code such as GEANT4 [18].

References

[1] EicRoot simulation framework, `http://svn.racf.bnl.gov/svn/eic/eicroot`.

[2] S. Roesler, R. Engel, and J. Ranft, "The Monte Carlo event generator DPMJET-III," in *Advanced Monte Carlo for radiation physics, particle transport simulation and applications. Proceedings, Conference, MC2000, Lisbon, Portugal, October 23-26, 2000*, pp. 1033–1038, 2000.

[3] A. Accardi *et al.*, "Electron Ion Collider: The Next QCD Frontier," *Eur. Phys. J.*, vol. A52, no. 9, p. 268, 2016.

[4] R. B. Palmer, "Energy Scaling, Crab Crossing, and the Pair Problem," *eConf*, vol. C8806271, pp. 613–619, 1988.

[5] T. Abe *et al.*, "Beam operation with crab cavities at KEKB," *Conf. Proc.*, vol. C070625, p. 1487, 2007. [,1487(2007)].

[6] K. Akai *et al.*, "Commissioning and Beam Operation of KEKB Crab RF System," in *RF superconductivity. Proceedings, 13th International Workshop, SRF 2007, Beijing, China, October 14-19, 2007*, 2007.

[7] P. B. et al, "Functional Specifications of the LHC Prototype Crab Cavity System," in *FP7 High Luminosity Large Hadron Collider Design Study*, 2013. CERN-ACC-NOTE-2013-003.

[8] G. Bassi, A. Blednykh, and V. Smaluk, "Self-consistent simulations and analysis of the coupled-bunch instability for arbitrary multibunch configurations," *Phys. Rev. Accel. Beams*, vol. 19, no. 2, p. 024401, 2016.

[9] W. Bruns,`http://www.gdfidl.de`.

[10] K. L. F. Bane and M. Sands, "The Short-Range Resistive Wall Wakefields," *AIP Conf. Proc.*, vol. 367, pp. 131–149, 1996.

[11] A. Blednykh, G. Bassi, Y. Hidaka, V. Smaluk, and G. Stupakov, "Low-frequency quadrupole impedance of undulators and wigglers," *Phys. Rev. Accel. Beams*, vol. 19, no. 10, p. 104401, 2016.

[12] A. Chao, S. Heifets, and B. Zotter, "Tune shifts of bunch trains due to resistive vacuum chambers without circular symmetry," *Phys. Rev. ST Accel. Beams*, vol. 5, p. 111001, 2002.

[13] J. Laslett in *in Proceedings of the Summer Study on Storage Rings, Brookhaven, 1963 (BNL, Brookhaven, NY, 1963)* , p. 324?367, 1963.

[14] Y. Luo *et al.*, "Beam-beam interaction, pre-cd erhic design report," 2018.

[15] A. Piwinski, "Beam losses and lifetime," 1985.

[16] C. Montag *et al.*, "Overview of the eRHIC Ring-Ring Design," in *Proceedings, 8th International Particle Accelerator Conference (IPAC 2017): Copenhagen, Denmark, May 14-19, 2017*, p. WEPIK049, 2017.

[17] "S. khan, unpublished."

[18] S. Agostinelli *et al.*, "GEANT4: A Simulation toolkit," *Nucl. Instrum. Meth.*, vol. A506, pp. 250–303, 2003.